JACS
JOURNAL OF THE AMERICAN CHEMICAL SOCIETY

Article

pubs.acs.org/JACS

Direct Investigation of Halogen Bonds by Solid-State Multinuclear Magnetic Resonance Spectroscopy and Molecular Orbital Analysis

Jasmine Viger-Gravel, Sophie Leclerc, Ilia Korobkov, and David L. Bryce*

Department of Chemistry and Center for Catalysis Research and Innovation, University of Ottawa, 10 Marie Curie Private, Ottawa, Ontario, Canada K1N 6N5

Supporting Information

ABSTRACT: Noncovalent interactions play a ubiquitous role in the structure, stability, and reactivity of a wide range of molecular and ionic cocrystals, pharmaceuticals, materials, and biomolecules. The halogen bond continues to be the focus of much attention, due in part to its strength and unique directionality. Here, we report a multifaceted experimental and computational study of halogen bonds in the solid state. A series of cocrystals of three different diiodobenzene molecules and various onium halide (Cl^- or Br^-) salts, designed to exhibit moderately strong halogen bonds (C—I···X^-) in the absence of competing hydrogen bonds, has been prepared and characterized by single-crystal X-ray diffraction. Interestingly, a wide range of geometries about the halide anion are observed. $^{35/37}$Cl and $^{79/81}$Br solid-state NMR spectroscopy is applied to characterize the nuclear quadrupolar coupling constants (C_Q) and asymmetry parameters (η_Q) for the halogen-bonded anions at the center of bonding environments ranging from approximately linear to distorted square planar to octahedral. The relationship between the halogen bond environment and the quadrupolar parameters is elucidated through a natural localized molecular orbital (NLMO) analysis in the framework of density functional theory (DFT). These calculations reveal that the lone pair type orbitals on the halogen-bonded anion govern the magnitude and orientation of the quadrupolar tensor as the geometry about the anion is systematically altered. In —C—I···X^-···I—C— environments, the value of η_Q is well-correlated to the I···X^-···I angle. ^{13}C NMR and DFT calculations show a correlation between chemical shifts and halogen bond strength (through the C—I distance) in *o*-diiodotetrafluorobenzene cocrystals. Overall, this work provides a chemically intuitive understanding of the connection between the geometry and electronic structure of halogen bonds and various NMR parameters with the aid of NLMO analysis.

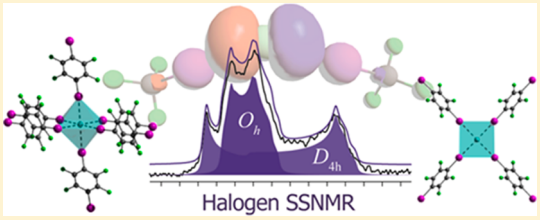

INTRODUCTION

Halogen bonds (XBs) are currently attracting much attention in the literature due to their multiple applications in diverse research fields, including crystal engineering[1,2] and biochemistry.[3,4] This class of noncovalent interaction continues to find applications in these varied areas of research, as halogen bonds can be comparable to or stronger (ranging from 1.2 kcal/mol for Cl···Cl interactions in chlorocarbons to 43 kcal/mol in I_3^-···I_2)[5] than hydrogen bonds (typically 3—7 kcal/mol)[6] and other noncovalent interactions such as anion—π,[6,7] cation—π,[8] and Lewis acid—Lewis base interactions.[6] Additionally, halogen bonds are highly directional and can align their components with specific orientations which are appealing in the architecture of supramolecular[9] or functional materials, such as anion—organic frameworks[10,11] and crystalline assemblies.[12,13] As for the biochemical relevance of halogen bonds, they have been observed in molecular recognition and folding processes and in ligand binding.[14−16] This has sparked interest in the development of new drugs,[17,18] where halogen bonds play a key role,[19] as well as in anion binding[20−24] and catalysis.[25]

The halogen bond (R—X···Y—Z) is defined as an electrostatic interaction between a halogen bond donor, an electrophilic region of a halogen atom (X), part of a molecule (R), which can be an organic or inorganic moiety or another halogen atom (acting as an electron withdrawing group), and a halogen bond acceptor, Y—Z, a nucleophilic region of another molecule, such as a Lewis base, halide, or π-electrons.[26] The electron-withdrawing group, R, will help generate a positive electrostatic potential along the far end of the R—X bond, known as the σ-hole, which is surrounded by negative electrostatic potential.[27,28]

Over the past decade in particular, halogen bonds have been extensively characterized with X-ray diffraction in the solid state.[29,30] Simultaneously, Legon and co-workers have made significant contributions to understanding halogen bonds in the gas phase.[31] They have examined experimentally how the structures of halogen-bonded complexes depend on the nature of the halogen and the Lewis base with the use of rotational spectroscopy. Among the parameters which can be extracted from such experiments are the halogen nuclear quadrupolar coupling constants, C_Q, which give quantitative information about the electric field redistribution associated with the halogen bonding process.[32,33]

Received: October 3, 2013
Published: May 1, 2014

   dx.doi.org/10.1021/ja5013239 | J. Am. Chem. Soc. 2014, 136, 6929−6942

The IUPAC definition of XBs states that the X···Y halogen bond usually leads to characteristic changes in the nuclear magnetic resonance signals of R—X and Y—Z.[26] In solution ^{1}H NMR studies, solvent shifts of haloformic protons have been monitored when halogen bonds are formed with various electron-rich solvents.[34] ^{13}C NMR has been used to detect, in a series of iodoalkynes, the effects of XB interactions on the $\delta_{iso}(^{13}C\alpha)$ value, which may vary by up to 15 ppm depending on the nature of the solvent.[35] Solution ^{19}F NMR has also been successfully applied to the determination of association constants of halogen bonding anion receptors, where the binding affinity of the receptor is a good parameter for describing selectivity, which is important in molecular recognition.[20,21] Erdélyi has used NMR to elegantly demonstrate that symmetric halogen bonding is preferred in solution in certain $[N{-}X{-}N]^{+}$ systems.[36] In the solid state, Weingarth and co-workers have determined N···I distances from ^{15}N−^{127}I dipolar coupling interactions through rotary resonance recoupling ^{15}N solid-state NMR (SSNMR) experiments.[37] Bouchmella et al. observed imidazolyl-containing haloalkenes and haloalkynes involved in halogen bonds by ^{1}H, ^{15}N, and ^{13}C SSNMR.[38] The ^{13}C NMR data were, however, inconclusive with respect to establishing a link between the halogen bond and the spectral data, as they were not able to observe the resonance for the carbon directly involved in the interaction. Our group has observed, in a series of XB compounds containing iodobenzenes, significant changes in the chemical shift (CS) tensors of the nuclei involved in the halogen bond in comparison to the starting material, which is devoid of the noncovalent interaction with multinuclear solid-state magnetic resonance.[39−41] Attrell and co-workers[42] studied a series of solid haloanilium halides where they used halogen SSNMR ($^{35/37}$Cl, $^{79/81}$Br, and ^{127}I)[43−50] as a probe to study the halogen bond acceptor. Due to competing hydrogen-bonding interactions in those compounds and the fact that the halogen bonds were weak, it was difficult to unambiguously correlate the NMR parameters to the halogen bonding environment. One of the open questions in characterizing halogen bonds concerns the understanding of how the NMR parameters of the nuclei involved in halogen bonds, particularly the halogens themselves, may be more rigorously related to (i) the local XB geometry and (ii) the local electronic structure; more specifically, the molecular orbitals (MOs) involved in the halogen bond.

In the present study, novel complexes have been synthesized to specifically have moderately strong halogen bonds, with R_{XB} values ranging between 0.79 and 0.91. The normalized distance parameter, $R_{XB} = d_{I\cdots X^-}/\sum d_{VdW}$, is the ratio of the distance between the halogen and the electron donor to the sum of the van der Waals radii of the atoms or ions involved, $\sum d_{VdW}$.[51] In addition, these cocrystals were designed to be devoid of competing interactions such as hydrogen bonding. The compounds used in this study contain iodoperfluorobenzenes, "now considered to be the 'iconic' halogen bond donors",[52] cocrystallized with different ammonium or phosphonium halide XB acceptors. In addition to characterization by single-crystal X-ray diffraction, comprehensive multinuclear solid-state magnetic resonance spectroscopic studies are reported. The origins of the observed NMR parameters, such as the quadrupolar coupling constant, C_Q, and asymmetry parameter, η_Q, are further examined with natural localized molecular orbital (NLMO) analyses.[53,54] NLMO analyses provide direct insight into the relationship between structure and spectral parameters by allowing one to identify contributions of individual occupied molecular orbitals (MOs) to the NMR interaction tensors.[55] This work therefore combines experimental and theoretical methods to provide insight into the relationship between the geometry and electronic structure of halogen bonds and their corresponding spectroscopic observables.

EXPERIMENTAL SECTION

Synthesis. Starting materials were purchased from Sigma-Aldrich and were used without further purification. At room temperature, an equimolar amount of *p*-diiodotetrafluorobenzene (*p*-DITFB, **1**), *o*-diiodotetrafluorobenzene (*o*-DITFB, **2**), or *p*-diiodobenzene (*p*-DIB, **3**) was dissolved in dichloromethane with an ammonium or phosphonium salt (*n*-Bu_4NCl (**A**), *n*-Bu_4PCl (**B**), *n*-Bu_4PBr (**C**), *n*-Bu_4NBr (**D**), Ph_4PCl (**E**), $EtPh_3PBr$ (**G**)), yielding the following halogen-bonded cocrystals: [(*n*-Bu_4NCl)(*p*-DITFB)] (**1A**),[77] [(*n*-Bu_4PCl)(*p*-DITFB)] (**1B**), [(*n*-Bu_4PCl)(*o*-DITFB)] (**2B**), [(Ph_4PCl)-(*p*-DITFB)] (**1E**), [(Ph_4PCl)(*o*-DITFB)]·$2CH_2Cl_2$ (**2E**), [(*n*-Bu_4PBr)(*p*-DITFB)] (**1C**), [(*n*-Bu_4NBr)(*p*-DITFB)] (**1D**), [(*n*-Bu_4PBr)(*o*-DITFB)] (**2C**), [($EtPh_3PBr$)(*p*-DITFB)] (**1G**), and [($EtPh_3PBr$)$_2$(*p*-DIB)] (**3G**). The preparation and crystal structures of some of the halogen-bonded compounds containing *p*-DITFB were previously reported.[39,77] The numbering used for the compounds is summarized in Table S1 of the Supporting Information.

Crystals of compounds **2B** and **1E** were obtained by slow evaporation from a minimum amount of dichloromethane. Crystals of compounds **2C**,**E** were obtained using a slow diffusion method. The compounds were dissolved in a minimum amount of dichloromethane and placed in a vial which was then placed in a jar containing hexane and sealed.

X-ray Crystallography. Data collection results for compounds **1E**, **2B**,**C**,**E**, **3G**, and *o*-DITFB represent the best data sets obtained in several trials for each sample. The crystals were mounted on thin glass fibers using paraffin oil. Prior to data collection, crystals were cooled to 200.15 K. Data were collected on a Bruker AXS SMART single-crystal diffractometer equipped with a sealed Mo tube source (wavelength 0.71073 Å) APEX II CCD detector. Raw data collection and processing were performed with the APEX II software package from Bruker AXS.[56] Diffraction data for **1E**, **2B**,**C**, **3G**, and *o*-DITFB were collected with a sequence of 0.5° ω scans at 0, 120, and 240° in φ. In order to ensure adequate data redundancy, diffraction data for **2E** were collected with a sequence of 0.5° ω scans at 0, 90, 180, and 270° in φ due to their lower symmetry. Initial unit cell parameters were determined from 60 data frames with a 0.3° ω scan, each collected for different sections of the Ewald sphere. Semiempirical absorption corrections based on equivalent reflections were applied.[57] Systematic absences in the diffraction data set and unit cell parameters were consistent with triclinic $P\bar{1}$ (No. 2) for compound **2E**, monoclinic $P2_1/c$ (No. 14) for compounds **2B**,**C**, monoclinic $P2_1/n$ (No. 14) for compound **3G** and *o*-DITFB, and monoclinic $C2/c$ (No. 15) for compound **1E**. Solutions in centrosymmetric space groups for all compounds yielded chemically reasonable and computationally stable results of refinement. The structures were solved by direct methods, completed with difference Fourier synthesis, and refined with full-matrix least-squares procedures based on F^2.

For compound **2E**, thermal motion parameters for atoms of two partially occupied CH_2Cl_2 solvent molecules suggested a positional disorder not related to the symmetry elements. The disorder was successfully modeled; however, a set of geometrical (SADI) and thermal motion (SIMU, DELU) restraints was applied to achieve acceptable molecular geometries and thermal motion values. Disordered fragment occupancies were refined with satisfactory results at 25%:25% for both CH_2Cl_2 solvent molecules.

In the structural models of **2B**,**C**,**E** and *o*-DITFB, all molecular fragments of the structures are located in general positions (i.e., not on symmetry elements). In the structure of **1E**, two molecules of *p*-$C_6I_2F_4$ are located on two different inversion centers, whereas all of the other structural fragments are situated in general positions. Similarly, one

dx.doi.org/10.1021/ja5013239 | J. Am. Chem. Soc. 2014, 136, 6929−6942

molecule of p-$C_6I_2H_4$ in the structure of **3G** also occupies an inversion center, with the rest of the moieties located in general positions. Further details on the refinements of the structural models for compounds **1E** and **2B** are given in the Supporting Information. In structural models for all compounds, hydrogen atoms were located from the differences in Fourier maps. However, after initial positioning, all hydrogen atoms were constrained to suitable geometries and subsequently treated as idealized contributions during the refinement. All scattering factors are contained in several versions of the SHELXTL program library, with the latest version being used (6.12).[58]

Solid-State NMR Spectroscopy. Carbon-13 and chlorine-35/37 SSNMR experiments were carried out on a 400 MHz (B_0 = 9.4 T) Bruker Avance III wide-bore spectrometer equipped with a triple-resonance 4 mm MAS probe and a 5 mm solenoid probe, respectively. ^{13}C, $^{35/37}$Cl, and $^{79/81}$Br SSNMR experiments were also carried out at the National Ultrahigh-field NMR Facility for Solids in Ottawa using a 21.1 T Bruker Avance II spectrometer equipped with either a Bruker 4 mm double-resonance MAS probe for ^{13}C or a home-built 5 mm solenoid probe for $^{35/37}$Cl and $^{79/81}$Br. Samples were powdered and packed in 4 mm o.d. zirconium oxide rotors for ^{13}C experiments and in 5 mm glass tubes for static $^{35/37}$Cl and $^{79/81}$Br experiments.

^{13}C SSNMR. Ramped amplitude ^{13}C cross-polarization (CP) MAS NMR[59] spectra were collected with SPINAL-64 ^{1}H decoupling[60] for all samples containing protons at two fields, 9.4 and 21.1 T (^{13}C Larmor frequencies of 100.613 and 226.338 MHz, respectively). Chemical shifts were referenced to solid glycine (δ_{iso}(^{13}C=O) 176.4 ppm with respect to TMS). The $\pi/2$ pulse length and contact times were 3.5 μs and 3 or 5 ms at 9.4 T and 2.5 μs and 3 ms at 21.1 T. Recycle delays ranged from 5 to 15 s. A single-channel rotor-synchronized Hahn-echo experiment (i.e., $\pi/2-\tau_1-\pi-\tau_2-$acq) was used for the acquisition of the spectrum of o-DITFB. Further details are provided in the Supporting Information.

$^{35/37}$Cl SSNMR. Chlorine chemical shifts and pulse widths were calibrated using the $^{35/37}$Cl NMR signal of KCl powder (δ_{iso}(KCl(s)) 8.54 ppm with respect to 0.1 M NaCl in D_2O). The CT-selective pulse widths were scaled by $1/(I + 1/2)$. Spectra were collected under stationary conditions at two fields (ν_L(^{35}Cl) = 39.204 MHz at 9.4 T and 88.194 MHz at 21.1 T; ν_L(^{37}Cl) = 32.634 MHz at 9.4 T and 73.412 MHz at 21.1 T). At 9.4 T, WURST-QCPMG[61] experiments combined with proton continuous wave (CW) decoupling to acquire $^{35/37}$Cl NMR spectra in combination with the variable offset cumulative spectrum (VOCS) method (100 kHz steps) were advantageous, as the nuclei of interest are dilute in the halogen-bonded complexes ($^{35/37}$Cl ranges from 6.29 to 33.1 mg/cm^3) and the spectra are broad.[62] A 50 μs WURST pulse with a 500 kHz bandwidth sweep from high to low frequency was used with pulse powers optimized experimentally (see the Supporting Information). The spikelet separation was set to 5 kHz by setting the echo duration to 106 μs with pulse ring-down times of 20 μs; 128 echoes were acquired in every scan. The recycle delays used for these compounds varied between 2 and 4 s. At 21.1 T, $^{35/37}$Cl SSNMR signals were acquired using an echo (i.e., $\pi/2-\tau_1-\pi/2-\tau_2-$acq)[63] pulse sequence combined with the VOCS method and CW proton decoupling. Typical acquisition parameters were CT-selective $\pi/2$ pulse lengths of 4 μs, spectral windows of 500 kHz, τ_1 values of 45 μs, pulse delays of 1 or 2 s, and 14k to 32k scans per piece.

$^{79/81}$Br SSNMR. The experimental setup, pulse calibration, and referencing were done using solid KBr (δ_{iso}(KBr(s)) 54.51 ppm with respect to 0.03 M NaBr in D_2O). The Larmor frequencies for bromine were ν_L(^{79}Br) = 225.518 MHz and ν_L(^{81}Br) 243.094 MHz at 21.1 T. The CT-selective $^{79/81}$Br pulses were 1.5 μs for the Solomon echo experiment used to acquire the SSNMR spectra. A recycle delay of 0.2 s, spectral window of 2 MHz, and transmitter offsets of 500 kHz were used. τ_1 varied between 18 and 175 μs, and each piece was collected with 14k to 24k scans.

Spectral Simulation and Processing. All NMR data were processed with Bruker TopSpin 3.0 software. Echoes were left-shifted where required. The WURST-QCPMG spectra were processed in magnitude mode. The first echo of each of the ^{37}Cl WURST-QCPMG data sets was omitted due to probe ringing. No apodization was used when processing these spectra. For the VOCS method, each piece was processed identically and coadded together to yield the final spectrum. Simulations were performed with WSolids1[64] and DMFIT (v.2011).[65] Simulations of ^{13}C NMR spectra included chemical shifts, line broadening, and the appropriate number of crystallographic sites determined by X-ray crystallography. Stack plots of the experimental and simulated spectra were prepared using DMFIT. Further information is given in the Supporting Information.

Computational Details. Models were generated from X-ray crystal structure atomic coordinates for each halogen-bonded compound using one halide ion and the nearest interacting p- or o-DITFB or p-DIB molecule(s) (see Scheme 1 and Figure 1). Only for

Scheme 1. General Halogen-Bonding Motif (X = Cl, Br) for 1A−D and 2B,C

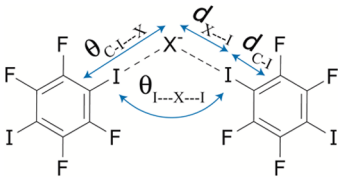

Cl2 (site A) of **1E** were the diiodotetrafluorobenzenes replaced by iodotrifluoromethane molecules to ensure convergence. The positions of the fluorine atoms in that model were optimized in Gaussian09[66] (B3LYP/3-21G). The NLMOs, electric field gradient (EFG) tensors, and magnetic shielding (MS) tensors were calculated with the Amsterdam Density Functional (ADF) program (version 2009.01). Scalar and spin−orbit relativistic effects were included using the zeroth-order regular approximation (ZORA). The revised Perdew, Burke, and Ernzerhof generalized gradient approximation exchange-correlation functional (GGA revPBE) of Zhang and Yang was used for all calculations.[67] The basis sets used for all atoms were Slater-type triple-ζ with polarization functions. A diffuse function was included in the basis set for the halide ion (i.e., AUG/ATZP),[68] whereas the basis set used for all other atoms was relativistically optimized (i.e., ZORA/TZP).[69]

The EFG and shielding tensors contained in the output files were analyzed using a modified version of the EFGShield program (version 1.1).[70] Magnetic shielding constants were converted to chemical shifts according to the formula $\delta_{ij} = (\sigma_{ref} - \sigma_{ij})/(1 - \sigma_{ref})$, where σ_{ref} is the absolute shielding constant of a reference compound (184.1 ppm for ^{13}C in TMS;[71] 974 ppm for $^{35/37}$Cl in infinitely dilute Cl^-(aq)).[72] To properly compare the calculated and experimental δ_{iso}($^{35/37}$Cl) values, we also accounted for the concentration of 0.1 M NaCl in D_2O[73] and the significant isotope shift of ∼5 ppm caused by D_2O.[74]

RESULTS AND DISCUSSION

X-ray Crystal Structures and Halogen Bond Geometry. Summarized in Table 1 are the crystallographic data for the new XB compounds, and in Table 2 are given the relevant halogen bonding distances ($d_{I\cdots X^-}$) and angles ($\theta_{C-I\cdots X^-}$) as well as the I···X$^-$···I angles ($\theta_{I\cdots X^-\cdots I}$) for the compounds studied presently (see Scheme 1). Also presented in Table 2 are the carbon−iodine bond lengths, which have been demonstrated to increase upon XB formation.[26] The crystal structures for XB compounds **1A−D,G** show a range of Cl$^-$···I and Br$^-$···I halogen bond environments and have been discussed previously.[39] We therefore focus the discussion below on crystallographic aspects of the new XB compounds. One measure of the presence of a halogen bond is when the distance between the halogen (i.e., I) and the electron donor (i.e., Cl$^-$ or Br$^-$) is shorter than the sum of their van der Waals radii (1.98 Å for covalent I and 1.81 and 1.96 Å for Cl$^-$ and Br$^-$,

dx.doi.org/10.1021/ja5013239 | J. Am. Chem. Soc. 2014, 136, 6929−6942

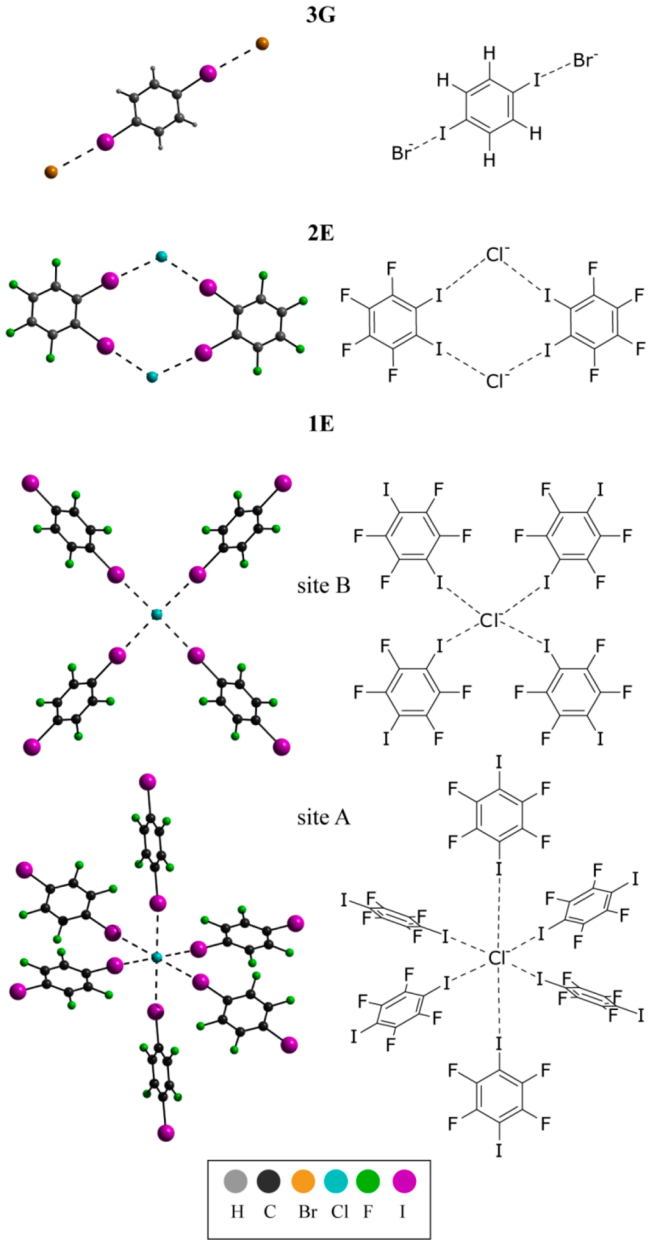

Figure 1. Local halogen-bonding geometries for some of the compounds studied in this work, from X-ray diffraction (left), and corresponding molecular structure schemes (right). Each atom is color coded: iodine is violet, chlorine is turquoise, bromine is orange, fluorine is green, carbon is black, and hydrogen is gray. Relative atom sizes are based on their relative van der Waals radii. See the angles and bond distances in Table 2. **1E** has two crystallographically distinct chloride sites, where the symmetries about sites A and B are almost perfectly octahedral and square planar, respectively. **3G** exhibits dianionic species of the form $[Br\cdots I{-}C_6H_4{-}I\cdots Br]^{2-}$. Cations are not shown.

respectively).[51] Also shown in Table 2 are the normalized distance parameters, R_{XB}, which range from 0.79 (**1A**) to 0.91 (**3G**). These values indicate the presence of moderately strong (**1A**) to weak (**3G**) halogen bonds. Very strong halogen bonds can have R_{XB} values as low as 0.69.[75] Generally, the R—X···Y angle tends to be linear in halogen bonds[26] (angles varying between 160 and 180°), as the halogen aligns with the *n* lone pair of electrons of the XB acceptor. All of the reported compounds exhibit near-linear halogen bonds, with angles ranging from 167.6 to 179.4° for $\theta_{C-I\cdots Cl^-}$, and 170.7 to 177.9° for $\theta_{C-I\cdots Br^-}$.

3G exhibits the same dianionic motif ($[Br\cdots I{-}C_6H_4{-}I\cdots Br]^{2-}$) as the previously described **1G**[39] (see Figure 1), as well as the same space group and crystal system ($P2_1/n$ and monoclinic). **3G** is the only reported compound in this study where the halogen donor molecule is *p*-diiodobenzene, and it exhibits the weakest XB interaction with an R_{XB} value of 0.91. This is attributed to the fact that protons are less electron withdrawing than fluorine; this leads to the formation of a smaller σ hole to interact with the halogen bond acceptor (Br^-).[28] The unit cell may be viewed in the Supporting Information in Figure S1, where it is observed that the dianionic species form discrete entities in alternating rows with PPh_3Et^+ cations which are associated two by two into an inversion-centered phenyl embrace motif. This motif has been observed for bulky phosphonium salt (i.e., Ph_3PR) derivatives[76] and was also observed in compound **1G**.[39]

Halogen-bonded compounds **2B,C** form one-dimensional architectures (see Figure S5 in the Supporting Information). Each halogen bond acceptor (Cl^- or Br^-) interacts with two iodine atoms, forming polymeric anionic zigzag chains as described for compounds **1A–D**[39] and by Abate et al.[77] Interestingly, for **2B** there are three crystallographically distinct chloride ion sites; the environment surrounding each halide is quite different, with $I\cdots Cl^-\cdots I$ angles of 112.0, 144.5, and 123.4° for Cl1, Cl2, and Cl3, respectively. One bromide site is present in **2C**, and the $I\cdots Br^-\cdots I$ angle is rather acute at 80.4°. Such acute angles have been observed previously by Grebe et al. in similar compounds.[78] **2B,C** both pack in the monoclinic crystal system with the $P2_1/c$ space group (see the Supporting Information for packing diagrams).

Compound **2E** packs in the triclinic crystal system and $P\bar{1}$ space group. Two molecules of *o*-DITFB and two chlorides interact together, as shown in Figure 1, where two halogen bond donors (I) interact with one halogen bond acceptor (Cl^-), forming a $I\cdots Cl^-\cdots I$ angle of 120.1°. In the unit cell along the *c* axis, there are two halogen-bonded complexes forming a row. These rows are separated by Ph_4P^+ cations associated two by two into an inversion-centered phenyl embrace motif (Figure S6, Supporting Information), as observed for **3G** and **1G**.[39,76] Dichloromethane molecules crystallize in the unit cell.

Finally, in **1E** ([(Ph_4PCl)(*p*-DITFB)]) there are two unique chloride sites in the crystal structure with two very different halogen-bonding environments and crystal networks. The first chloride site is at the center of a distorted-square-planar motif, where four different XB donor molecules interact with a single chloride anion (see Figure 1). These form infinite one-dimensional networks along the *c* axis (see the Supporting Information). The second chloride site sits at the center of a distorted octahedron by interacting with six iodine atoms (Figure 1) and forms a secondary intrinsic two-dimensional network (see the Supporting Information). In **1E**, when both chloride sites are observed, they alternate rows along the *b* axis (Supporting Information). Looking at the overall structure along the *c* axis, the Ph_4P^+ cation forms columns with the halide, which alternates rows with *p*-DITFB molecules.

The C–H hydrogen atoms in the onium counterions are well-removed from the coordination spheres of the halide ions in all compounds. Aliphatic CH–chloride contacts typically cluster around 2.39 Å,[79] whereas most of the shortest H–anion distances in the compounds studied here are around 3 Å.

dx.doi.org/10.1021/ja5013239 | J. Am. Chem. Soc. 2014, 136, 6929–6942

Table 1. Crystallographic Data and Selected Data Collection Parameters

	2B	2E[a]	2C	1E	3G
empirical formula	$C_{66}H_{108}Cl_3F_{12}I_6P_3$	$C_{31}H_{22}Cl_3F_4I_2P$	$C_{22}H_{36}BrF_4I_2P$	$C_{42}H_{20}ClF_{12}I_6P$	$C_{46}H_{44}Br_2I_2P_2$
formula wt	2090.18	861.60	741.19	1580.40	1072.37
cryst size, mm	0.27 × 0.23 × 0.11	0.21 × 0.14 × 0.14	0.24 × 0.18 × 0.10	0.21 × 0.17 × 0.15	0.24 × 0.20 × 0.17
cryst syst	monoclinic	triclinic	monoclinic	monoclinic	monoclinic
space group	$P2_1/c$	$P\bar{1}$	$P2_1/c$	$C2/c$	$P2_1/n$
Z	4	2	4	8	2
a, Å	13.4256(3)	11.8135(2)	13.1132 (4)	18.5756(2)	9.24230(10)
b, Å	25.3718(6)	12.8379(3)	15.1457(5)	19.3258(2)	12.5396(2)
c, Å	25.3449(6)	13.4744(3)	14.4157(5)	26.4008(3)	18.5824(3)
α, deg	90.00	92.2880(10)	90.00	90.00	90.00
β, deg	98.915(2)	114.0890(10)	98.7470(10)	99.1840(10)	98.3230(10)
γ, deg	90.00	104.8300(10)	90.00	90.00	90.00
V, Å^3	8529.0(3)	1779.12(7)	2829.78(16)	9356.08(18)	2130.92(5)
R_1(ref)	0.1716	0.0390	0.0289	0.0366	0.0228
wR_2(ref)	0.1541	0.1208	0.0604	0.0763	0.0520

[a] **2E** is a solvate.

Table 2. Selected Intermolecular Contact Distances, Angles, and Halogen Bonding Environment Surrounding the Halides in Halogen-Bonded Compounds[a]

compd		#I[b]	d_{I-C}/Å	$d_{I\cdots X^-}$ /Å	R_{XB}[c]	$\theta_{C-I\cdots X^-}$/deg	$\theta_{I\cdots X^-\cdots I}$ /deg	$I_x\cdots X^-\cdots I_y$
1A[d]		1	2.1071	2.988	0.79	178.1	109.1	$I_1\cdots Cl^-\cdots I_2$
		2	2.0963	3.104	0.82	170.2		
1B[d]		1	2.0946	3.038	0.80	175.0	155.7	$I_1\cdots Cl^-\cdots I_2$
		2	2.1022	2.976	0.79	177.0		
2B								
	Cl1	1	2.1152	3.157	0.84	175.8	112.0	$I_3\cdots Cl^-\cdots I_2$
		2	2.0965	3.088	0.82	175.3	144.5	$I_1\cdots Cl^-\cdots I_6$
	Cl2	3	2.1173	3.115	0.83	178.0	123.4	$I_5\cdots Cl^-\cdots I_4$
		4	2.115	3.150	0.83	174.9		
	Cl3	5	2.0948	3.052	0.81	169.6		
		6	2.0874	3.062	0.81	176.8		
1E								
	Cl1	1	2.0931	3.204	0.85	174.4	91.6	$I_1\cdots Cl^-\cdots I_2$
		2	2.0952	3.240	0.86	167.6	75.7	$I_2\cdots Cl^-\cdots I_3$
	Cl2	3	2.0653	3.332	0.88	174.6	100.4	$I_1\cdots Cl^-\cdots I_3$
		4	2.0872	3.191	0.85	179.4	176.3	$I_4\cdots Cl^-\cdots I_5$
		5	2.0944	3.204	0.85	176.1		
		6	2.0925	3.204	0.85	174.5		
2E[e]		1	2.1058	3.132	0.83	177.4	120.1	$I_1\cdots Cl^-\cdots I_2$
		2	2.1065	3.152	0.83	176.1		
1D[d]		1	2.1121	3.166	0.83	175.3	139.2	$I_1\cdots Br^-\cdots I_2$
		2	2.0963	3.236	0.84	177.9		
1C[d]		1	2.1046	3.189	0.83	176.8	140.9	$I_1\cdots Br^-\cdots I_2$
		2	2.0995	3.196	0.83	177.7		
2C		1	2.1085	3.347	0.87	174.6	80.4	$I_1\cdots Br^-\cdots I_2$
		2	2.1047	3.269	0.85	174.1		
1G[d]		1	2.1081	3.147	0.82	175.5		
3G		1	2.1125	3.472	0.91	170.7		

[a] Refer to Scheme 1 for information on the reported angles and distances. [b] #I refers to crystallographically different iodine atoms in each of the structures. [c] R_{XB} is the normalized distance parameter, $R_{XB} = d_{I\cdots X^-}/\sum d_{VdW}$, where $d_{I\cdots X^-}$ is the shortest contact distance between the halogen and the halide and d_{VdW} is the sum of their van der Waals radii (1.98 Å for I and 1.81, 1.96 Å for Cl^- and Br^-, respectively).[51] [d] Crystal structure reported in ref 39. [e] Disordered solvate (DCM).

Solid-State NMR Spectroscopy: Correlation of NMR Data with Local Structure. *^{13}C NMR.* The ^{13}C CP/MAS NMR spectra of **1E**, **2B**,**C**, and **3G** corresponding to the region of the carbons covalently bonded to iodine are shown in Figure 2. Analogous spectra of the pure non-halogen-bonded aromatic compounds (*o*-DITFB, *p*-DITFB, *p*-DIB) are also shown. The chemical shifts, which were obtained by simultaneously fitting the spectra at magnetic fields of 9.4 and 21.1 T, are summarized in Table 3. The full ^{13}C CP/MAS NMR spectra and chemical shift assignments may be found in the Supporting Information. As previously described,[39] such spectra are challenging to acquire due to possible relaxation caused by the directly bonded

dx.doi.org/10.1021/ja5013239 | J. Am. Chem. Soc. 2014, 136, 6929−6942

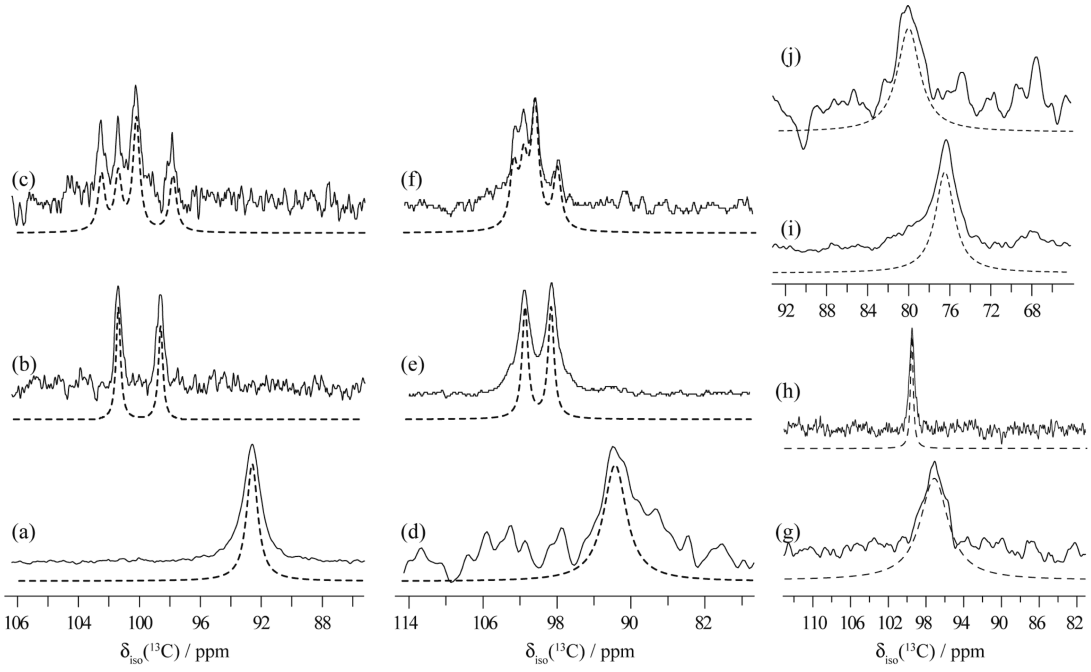

Figure 2. Selected regions of the experimental (solid lines) and simulated (dashed lines) ^{13}C CP/MAS SSNMR spectra of (a, d) *o*-DITFB, (b, e) **2C**, and (c, f) **2B** recorded at 21.1 T (left, a–c) and 9.4 T (middle, d–f) and of (g) *p*-DIB, (h) **3G**, (i) *p*-DITFB (this spectrum was also shown in ref 39), and (j) **1E**, recorded at 21.1 T (right). In the case of **2B**, the intensities of the lines in the simulations were adjusted to match the experimental data. This accounts in an ad hoc manner for partial overlap of unresolved resonances and possible small differences in site intensities due to differential cross-polarization efficiencies.

Table 3. Experimental ^{13}C Isotropic Chemical Shifts of Carbons Covalently Bonded to Iodine

	compd	$\delta_{iso}(^{13}C)$/ppm[a]
	o-$C_6F_4I_2$	92.6(1.3)
	p-$C_6H_4I_2$	97.1(2.6)
2C	[(*n*-Bu_4PBr)(*o*-$C_6F_4I_2$)]	98.6(0.4)
		101.4(0.4)
2B[b]	[(*n*-Bu_4PCl)(*o*-$C_6F_4I_2$)]	102.5(0.3)
		101.4(0.3)
		100.2(0.5)
		97.9(0.2)
3G	[($EtPh_3PBr$)$_2$(*p*-$C_6H_4I_2$)]	99.5(0.5)
1E[b]	[(Ph_4PCl)(*p*-$C_6F_4I_2$)]	80.2(1.5)

[a]Experimental ^{13}C isotropic chemical shift of the carbon covalently bonded to iodine. Errors are given in parentheses, which are equal to the line width at half-height. [b]For **2B** and **1E**, six distinct carbon sites are expected for each, from X-ray crystallography.

iodine, nearby fluorines causing dipolar broadening, and distant protons rendering CP inefficient. The use of a 21.1 T spectrometer was essential to resolve some of the chemical shifts observed for the carbons involved in the weak XB interaction. The residual dipolar coupling (RDC) between a spin $^1/_2$ nucleus such as ^{13}C and a quadrupolar nucleus such as ^{127}I is reduced at higher magnetic fields, as is apparent when the line widths observed at 9.4 T are compared to those measured at 21.1 T (~125 vs ~90 Hz). No splitting or asymmetric broadening attributable to RDC is observed, and spectra at both fields were fit with consistent chemical shift values. A calculation using typical parameters for the ^{127}I–^{13}C dipolar coupling constant (657 Hz) and the ^{127}I quadrupolar coupling constant (1000 MHz) gives a residual dipolar coupling constant of about −1.1 kHz at 21.1 T. A spectral simulation based on these values shows that a fully ^{127}I coupled ^{13}C multiplet line shape should span about 12 ppm at 21.1 T, suggesting that the ^{13}C line shapes obtained presently are at least partially ^{127}I self-decoupled.

Higher ^{13}C chemical shifts are observed to generally correlate with longer C–I bonds in the halogen-bonded *o*-DITFB compounds. The values of $\delta_{iso}(^{13}C)$ for the C–I carbons in **2C** (98.6(0.4) and 101.4(0.4) ppm) and **2B** (102.5(0.3), 101.4(0.3), 100.2(0.5), and 97.9(0.2) ppm) are all significantly larger than that for pure *o*-DITFB, where no XB is present (92.6(1.3) ppm). This is consistent with the trend noted for halogen-bonded *p*-DITFB compounds.[39] The substantially lower chemical shift observed for the carbon bonded to iodine in comparison to the typical chemical shift of carbons in aromatic rings is due to a relativistic spin-orbit-induced heavy atom substituent effect; the magnitude of the relativistic shift is largely due to the magnitude of the spin–orbit splitting of the heavy atom and tends to increase with the valence s orbital character of the observed nucleus.[80] However, a precise correlation between d_{C-I} and $\delta_{iso}(^{13}C)$ cannot be established for the halogen-bonded *o*-DITFB compounds, since for two out of the four compounds studied here, not all of the isotropic peaks of the different crystallographically distinct carbons are resolved. In the case of **2B**, six nonequivalent carbons are expected from the crystal structure and only four resonances are resolved in the NMR spectra at both fields (Figure 2c,f).

The ^{13}C resonance of the halogen-bonded complex **3G** is more deshielded ($\delta_{iso}(^{13}C)$ 99.5(0.5) ppm) in comparison to pure *p*-DIB (Figure 2g) (97.1(2.6) ppm). In this example, the increase in chemical shift upon halogen bonding may be clearly correlated to an increased carbon–iodine distance (d_{C-I} = 2.09635 and 2.1125 Å for *p*-DIB and **3G**, respectively) found from X-ray data, since only one distinct carbon site is present for both the XB compound and the starting material.

dx.doi.org/10.1021/ja5013239 | J. Am. Chem. Soc. 2014, 136, 6929–6942

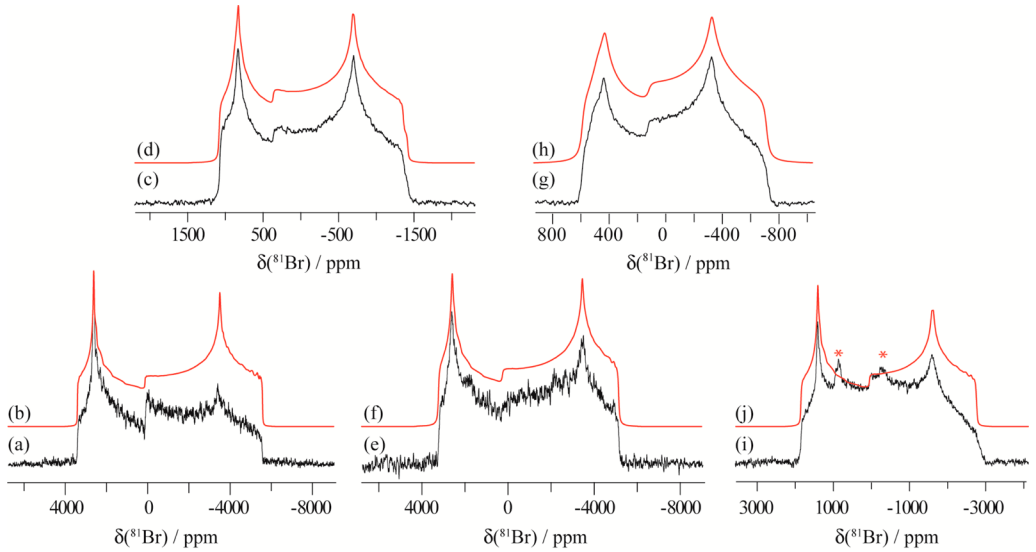

Figure 3. ^{81}Br solid-state NMR spectra of stationary powdered halogen-bonded compounds acquired at 21.1 T. Experimental spectra are shown in (a) **1D**, (c) **2C**, (e) **1C**, (g) **3G**, and (i) **1G**, and their respective simulated spectra are given in (b), (d), (f), (h), and (j). Asterisks in (i) mark an impurity.

Table 4. Experimental ^{81}Br EFG and CS Tensor Parameters for Halogen-Bonded Compounds[a]

	$\lvert C_Q(^{81}Br)\rvert$/MHz[b]	η_Q[b]	δ_{iso}/ppm[c]	Ω/ppm[c]	κ[c]	α/deg	β/deg	γ/deg
1D	58.0(0.2)	0.22(0.01)	250(6)	255(20)	1.0(0.2)	0(0)	0(0)	90(20)
1C	57.0(0.2)	0.19(0.01)	310(10)	110(10)	0.9(0.3)	0(0)	20(10)	90(0)
2C	30.8(0.1)	0.27(0.01)	256(4)	192(10)	0.0(0.1)	34(4)	82(2)	12(2)
1G	40.7(0.1)	0.26(0.01)	210(10)	320(20)	0.9(0.1)	0(20)	5(1)	90(40)
3G	21.5(0.1)	0.32(0.01)	140(10)	115(15)	−0.9(0.2)	90(2)	0(5)	30(5)

[a]Error bounds are given in parentheses. [b]The EFG tensor, **V**, can be diagonalized to provide three principal components defined as $|V_{33}| \geq |V_{22}| \geq |V_{11}|$. The quadrupolar coupling constant, C_Q, is equal to eQV_{33}/h; the asymmetry parameter, η_Q, is equal to $(V_{11} - V_{22})/V_{33}$. While C_Q may take any real value, only $|C_Q|$ can be measured from conventional SSNMR experiments. [c]The isotropic chemical shift, δ_{iso}, is equal to $(\delta_{11} + \delta_{22} + \delta_{33})/3$, the span, Ω, is equal to $\delta_{11} - \delta_{33}$, and the skew, κ, is equal to $3(\delta_{22} - \delta_{iso})/\Omega$, where $\delta_{11} \geq \delta_{22} \geq \delta_{33}$.

Compound **1E** should have a total of six distinct carbon sites which are involved in halogen bonds. In spectra recorded at fields of 9.4 and 21.1 T, only one very broad peak is observed; hence, none of the chemical shifts can be resolved (Figure 2j). However, it is clear that the carbon isotropic chemical shift of the halogen-bonded complex is deshielded with respect to *p*-DITFB, as was previously observed for **1A**−**D**,**G**.[39] This follows the overall trend, even though a site-specific correlation with the six different C−I distances cannot be established.

$^{79/81}$Br NMR. Compounds with a bromide anion as halogen bond acceptor have been characterized with $^{79/81}$Br SSNMR at 21.1 T (see Figure 3 and the Supporting Information). The bromine NMR parameters summarized in Table 4 were obtained by simultaneously simulating the NMR spectra of both bromine isotopes when possible. These spectra span several MHz due to second-order quadrupolar broadening. Attempts to acquire these spectra at moderate magnetic fields of 9.4 and 11.75 T were impractical due to the combined effect of the large breadth of the spectra and the bromide concentration being quite low for $^{79/81}Br^-$, ranging from 23 mg/cm^3 (**2C**) to 64 mg/cm^3 (**3G**).

The ^{81}Br quadrupolar coupling constants for this series of halogen-bonded compounds vary from 21.5(0.1) MHz for **3G** to 58.0(0.2) MHz for **1D**. These values are an order of magnitude greater than the values for the pure bromide starting materials: i.e., ammonium and phosphonium bromide salts.[45,81] Generally, less symmetric electronic environments will correlate with larger C_Q values. They are in the same range ($C_Q(^{81}Br)$ = 12.3−45.3 MHz) as the values reported by Attrell et al. for halogen-bonded haloanilium halides.[42] The ^{81}Br isotropic chemical shifts are within the known range for bromides,[44] ranging from 140(10) to 310(10) ppm, and the CS tensor spans range from less than 110(10) ppm to 320(20) ppm.

Compounds **1D**,**C** are isostructural and feature polymeric anionic chains with $\theta_{I\cdots Br^-\cdots I}$ angles of 139.2 and 140.9°, respectively. Two polymorphs are known for **1D**: that of Metrangolo et al.[77] crystallizes in the space group *C*2/*c*, whereas our group reported the space group *Pccn*.[39] Compound **1C** also packs in the space group *C*2/*c*. These halogen-bonded compounds are characterized by similar ^{81}Br EFG tensor parameters (Table 4): $|C_Q(^{81}Br)|$ values of 58.0(0.2) and 57.0(0.2) MHz and η_Q values of 0.22(0.01) and 0.19(0.01) for **1D**,**C**, respectively. At higher magnetic field, bromine chemical shift anisotropy (CSA) contributes significantly to the NMR line shapes (Figure 3a,e; the span, Ω, is 255(20) ppm for **1D** and 110(10) ppm for **1C**; see also Figure S14 in the Supporting Information). The halogen-bonded compound **2C** also forms polymeric anionic zigzag chains, but with acute I···Br$^-$···I angles (80.4°) and packs in the space group $P2_1/c$. Qualitatively, this compound gives a much narrower ^{81}Br NMR line shape, which is quantified by a $|C_Q(^{81}Br)|$ value of 30.8(0.1) MHz (Figure 3g). This value may be related to the local halogen bonding environment (vide infra). Bromine CSA parameters for **2C** are between the values reported for **1C**,**D**: e.g., a span, Ω, of

dx.doi.org/10.1021/ja5013239 | J. Am. Chem. Soc. 2014, 136, 6929−6942

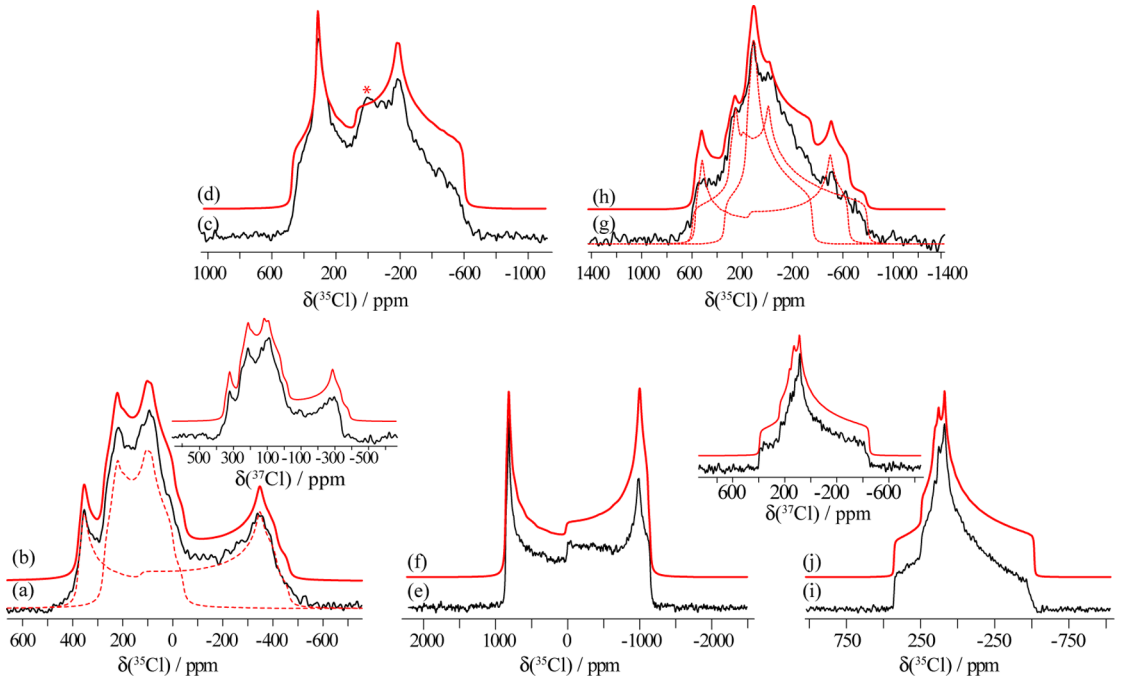

Figure 4. ^{35}Cl solid-state NMR spectra of static powdered halogen-bonded compounds acquired at 21.1 T. Experimental spectra are shown in (a) **1E**, (c) **2E**, (e) **1B**, (g) **2B**, and (i) **1A**, and their simulated spectra are in (b), (d), (f), (h), and (j), respectively. The residual Ph_4PCl in (c) is marked by a red asterisk. There are two crystallographically distinct sites in compound **1E** (a) and three crystallographically distinct sites in **2B** (g) (simulations shown with dashed lines). Shown in the insets are the experimental and simulated ^{37}Cl NMR spectra recorded at 21.1 T for (a) **1E** and (i) **1A**.

Table 5. Experimental ^{35}Cl EFG and CS Tensor Parameters for Halogen-Bonded Compounds[a]

		$\lvert C_Q(^{35}Cl)\rvert$/MHz	η_Q	δ_{iso}/ppm	Ω/ppm	κ	α/deg	β/deg	γ/deg
1A		5.43(0.05)	1.00(0.01)	117(3)	94(4)	−0.3(0.2)	0(5)	0(8)	106(4)
1B		10.42(0.04)	0.07(0.01)	132(4)	180(15)	0.85(0.10)	35(30)	2(2)	45(20)
2B[b]									
	site 1	4.57(0.20)	1.00(0.04)	112(10)	<60				
	site 2	8.22(0.30)	0.12(0.04)	148(20)	<60				
	site 3	7.15(0.05)	0.70(0.04)	135(20)	<60				
1E[c]									
	site 1	3.66(0.10)	0.38(0.04)	177(8)	60(15)	−0.4(0.2)	120(20)	106(16)	35(10)
	site 2	6.85(0.10)	0.12(0.02)	98(4)	96(10)	0.0(0.2)	0(10)	90(10)	40(10)
2E		6.77(0.20)	0.44(0.04)	94(10)	60(20)	1.00(0.04)		5(4)	

[a]Error bounds are given in parentheses. See also footnotes *b* and *c* of Table 4. [b]Three crystallographically distinct chlorine sites were determined from the X-ray diffraction structure. The asymmetry parameter is characteristic of the halogen-bonding environment, and each site may be assigned to the corresponding chloride. Details of the assignment are given in the main text. No CSA is incorporated in these fits to avoid overinterpretation of the NMR spectrum. [c]Two crystallographically distinct chlorine sites are present in the crystal structure of **1E**. The chloride in the pseudo-O_h geometry was assigned as Cl1, as the C_Q value is the smaller value that is expected for a quadrupolar nucleus in a symmetric environment. The second site has a larger C_Q value, in agreement with its square-planar geometry.

192(10) ppm. To improve the precision of the reported quadrupolar and CS tensor parameters, ^{79}Br NMR spectra of compounds **1D** and **2C** were also acquired and are shown in the Supporting Information.

Two dianionic bromide-containing species, **3G** and **1G**, are isostructural and pack in the same space group, $P2_1/n$. Their ^{81}Br NMR spectra are shown in Figure 3g,i. As stated above, compound **3G** exhibits a much weaker halogen bond in comparsion to **1G**. This difference is reflected in their respective ^{81}Br EFG and CSA parameters. For example, the value of $\lvert C_Q(^{81}Br)\rvert$ for **3G** (21.5(0.1) MHz) is half the value observed for **1G** (40.7(0.1) MHz). The smaller value of C_Q for **3G** may be qualitatively rationalized by considering that the bromide anion in this compound is much further removed from the nearby iodine, and its local electronic environment more closely approximates that of an isolated Br^- anion, for which the value of C_Q is 0. The asymmetry parameters are similar, with values of 0.26(0.01) and 0.32(0.01) for **1G** and **3G**, respectively. In addition, the more weakly halogen bonded complex **3G** has a smaller bromine chemical shift (140(10) ppm) and span (115(15) ppm) in comparison to **1G** (δ_{iso} 210(10) ppm and Ω = 320(20) ppm), corroborating the trend reported by Attrell et al.[42]

$^{35/37}$Cl SSNMR. Presented in Figure 4 are the ^{35}Cl NMR spectra (21.1 T) of the halogen-bonded complexes in which the halogen bond acceptor is a chloride anion. The spectra acquired at 9.4 T for ^{35}Cl and ^{37}Cl are shown in Figures S15 and S16 in the Supporting Information, respectively. The ^{35}Cl EFG and

dx.doi.org/10.1021/ja5013239 | J. Am. Chem. Soc. 2014, 136, 6929−6942

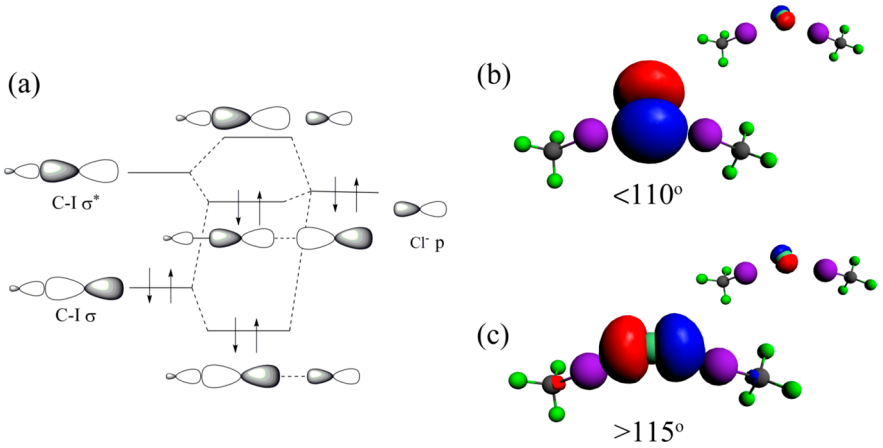

Figure 5. (a) Simplified molecular orbital diagram for a halogen bond between a C—I moiety and a chloride ion (after Pinter et al.[85]). (b, c) NLMO contributions to the largest principal component of the ^{35}Cl EFG tensor in a model halogen-bonded system (F_3C—I···Cl^-···I—CF_3). In (b) the lone pair orbital for chloride is represented for I···Cl^-···I angles less than or equal to 110°, and the inset gives the representation of the less important core orbital NLMO. In (c) is the chlorine lone pair orbital for $\theta_{I\cdots Cl^-\cdots I} \geq 115°$, and in the inset the core orbital is presented. The lone pair orbitals dominate the resulting EFG.

CS tensor parameters are presented in Table 5 and were obtained by simultaneously modeling the NMR spectra of both chlorine isotopes at two magnetic fields.

The ^{35}Cl quadrupolar coupling constants range from 3.66(0.10) MHz for **1E** to 10.42(0.04) MHz for **1B**. The largest of these values is slightly greater than that observed previously[42] for more weakly halogen bonded compounds. The chloride compounds in this study are moderately strongly halogen bonded, with R_{XB} values ranging from 0.79 to 0.88. The asymmetry parameters vary across the entire range of possible values, from 0.07(0.01) for **1B** to 1.00(0.01) for **1A**. Spectra of the halogen-bonded complexes were simulated with CSA, where the effect is more prominent at 21.1 T; however, due to the small magnitudes of the anisotropies and small overall range in their values, no clear correlation with any structural element is noted. The chlorine isotropic chemical shifts range from 98(4) to 177(8) ppm and the spans range from 60(15) ppm for **1E** to 180(15) ppm for **1B**, which are within the known range of values for chloride ions in nonsymmetric environments.[43,49,82,83]

The chlorine EFG tensor parameters may be related to the chloride anion halogen-bonding environment and to the local electronic structure (vide infra). First, consider the spectrum of **1E**, where two crystallographically nonequivalent chlorine sites are present, shown in Figure 4a. From the NMR line shape, the two different sites are clearly differentiated, as shown by the spectral deconvolution. It is possible to resolve multiple sites from a spectrum of quadrupolar nuclei, as the quadrupolar coupling constant is dependent on the coordination environment. When the coordination environment surrounding the nuclide is spherically symmetric, the C_Q value will be null and any divergence from that symmetry will cause an increase in C_Q.[84] In **1E**, chlorine site 1 (Cl1) is in a nearly octahedral geometry according to the X-ray crystal structure. This site may be assigned to the narrower ^{35}Cl NMR powder pattern with the smaller $|C_Q(^{35}Cl)|$ value of 3.66(0.10) MHz. The second chlorine site is in a pseudo-square-planar geometry and may be assigned to the broader ^{35}Cl line shape characterized by a quadrupolar coupling constant of 6.85(0.10) MHz (this assignment is supported by DFT calculations; vide infra). Compounds **2B** and **1A,B** have similar halogen bonding environments where one chloride anion interacts with two iodine atoms, thereby forming infinite linear polymeric anionic chains. **1A,B** have very similar structures and only differ by their cation, *n*-Bu_4N^+ or *n*-Bu_4P^+, respectively; they additionally pack in the same space group, $P2_1/c$. This change in cation is accompanied by a change in the angle surrounding the halide: $\theta_{I\cdots Cl^-\cdots I}$ = 109.1° for **1A** and 155.7° for **1B**. This interesting feature in their structures might explain the very different line shapes observed for these halogen-bonded compounds (see Figure 4e,i), as will be demonstrated through an NLMO analysis (vide infra). The $|C_Q(^{35}Cl)|$ value for **1A** (5.43(0.05) MHz) is about half that for **1B** (10.42(0.04) MHz). Even more intriguing, the asymmetry parameters take on two limiting values where in **1A** two spectral discontinuities ("horns") collapse with an η_Q value equal to 1 (1.00(0.01)) and for **1B** we distinctly see the two horns where the asymmetry parameter approaches 0 (0.07(0.01)).

Compound **2B** exhibits three crystallographically distinct chloride sites in the unit cell. They all have similar halogen bonding environments, where one chloride anion interacts with two halogen bond donors, forming a one-dimensional network (Figure S5 in the Supporting Information). However, from the ^{35}Cl NMR spectrum (see Figure 4g), it is not directly obvious how to assign the three powder patterns to the three crystallographic sites (vide infra).

Discussion: NLMO Analysis of the Halide Quadrupolar Coupling Tensors in the Context of the Experimental NMR and X-ray Data. The origins of the quadrupolar interaction at the halide nuclei as a result of the formation of a halogen bond may be intuitively grasped by considering a standard molecular orbital diagram (Figure 5a, after Pinter et al.[85]). Interaction of a halide lone pair (represented here by a p orbital) with the σ^* orbital of the carbon—iodine bond results in a halogen bond. It is the polarization of this same p orbital which gives rise to the quadrupolar interaction at the halide nucleus. While this qualitative picture is useful, ZORA DFT computations were carried out to provide a more theoretically rigorous insight into the relationship between the local environment of the halogen bond acceptor and the observed NMR parameters. The calculations are used to analyze the contributions of key molecular orbitals to the halide EFG

dx.doi.org/10.1021/ja5013239 | J. Am. Chem. Soc. 2014, 136, 6929−6942

tensors, through an NLMO analysis.[53−55] The theoretical basis of this analysis has been described and applied by Autschbach et al.[53] One of this method's advantages is that it provides an interpretation of the NMR parameters in terms of orbitals which are familiar to chemists (e.g., lone pairs, bonding orbitals, and core functions). Here, a model composed of two molecules of iodotrifluoromethane halogen-bonded with a chloride anion, where the I···Cl⁻···I angle was varied between 85 and 180° in 5° increments, was employed. The calculated value of V_{33} was chosen for more in-depth analysis, as it determines the value of the chlorine quadrupolar coupling constant. The major NLMO contributions to V_{33}(^{35}Cl) as core and lone-pair orbitals are presented in the Supporting Information.

Plotted in Figure 6a are the calculated ^{35}Cl principal components of the EFG tensor as a function of the I···Cl⁻···I

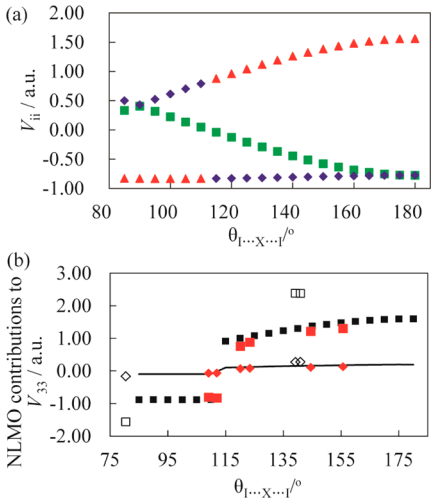

Figure 6. (a) Plot of the calculated EFG tensor components (where V_{33} are the red triangles, V_{22} are the green squares, and V_{11} are the blue diamonds, with $|V_{33}| \geq |V_{22}| \geq |V_{11}|$) for ^{35}Cl in a F_3C–I···Cl⁻···I–CF_3 model system where the I···Cl⁻···I angle is varied. (b) Plot of the NLMO contributions to the largest principal component V_{33} as a function of $\theta_{I\cdots Cl^-\cdots I}$, where the solid black squares represent the contributions from the chlorine lone pair orbitals and the black line represents the contributions from the chlorine core orbitals (see the Supporting Information). Overlaid on this plot are the values of the calculated contributions for the experimental halogen-bonded complexes (values from Table 6). In red are data for the chloride compounds (squares, lone pair NLMOs; diamonds, core NLMOs), showing excellent agreement with the data for the model system. The corresponding data for the bromide compounds are shown as empty squares and diamonds; as expected, the values are larger than those for chloride due to differences in geometries, unit cell volumes, and Sternheimer antishielding factors.

angle. A change in sign of the principal components V_{11} and V_{33} is evident for angles exceeding the tetrahedral angle of about 110°. From the calculations it is possible to determine the orientation of the EFG tensor, which has been plotted in Figure S18 of the Supporting Information for three I···Cl⁻···I angles of interest: 110, 115, and 180°. At $\theta_{I\cdots Cl^-\cdots I}$ = 110°, the eigenvector corresponding to V_{33} lies in the I···Cl⁻···I plane and bisects the $\theta_{I\cdots Cl^-\cdots I}$ angle. Around 115°, the eigenvector reorients to lie close to the I···Cl⁻ internuclear vector, and finally at 180° it is completely aligned with the I···Cl⁻···I axis. When the NLMO contributions to V_{33} are examined, two main types of MOs centered on the chloride anion dominate: core orbitals and lone pair orbitals. From the plot shown in Figure 6b, one can see that the contributions from the sum of the chloride core orbitals are minor (black line) and do not vary significantly between 80 and 180°. The same can be observed qualitatively from a plot of these core orbitals (Figure 5). Conversely, the contributions to V_{33} from the sum of the chloride ion lone pair NLMOs are more important: the same change in sign is observed between the angles 110 and 115° as for V_{33} (black squares). Additional details as well as each contributing lone pair orbital have been tabulated and plotted in the Supporting Information. Examination of the lone pair NLMO which largely determines the value of V_{33} in Figure 5b,c reveals that the main contributing orbital changes at ∼115°. At 115° and for larger angles, the principal axis of the orbital is aligned with the iodine atom; this corresponds to the localized orbital which is responsible for the halogen bond. To put this in the context of more familiar orbital types, consider again the MO diagram in Figure 5a, which depicts explicitly the chloride p orbital involved in the halogen bond. This p orbital may be readily identified with the p-type NLMO resulting from our DFT calculations and shown in Figure 5c, thus providing an intuitive understanding of the connection among the simple MO diagram, the NLMO analysis, and the resulting NMR parameters.

Additionally, when the I···Cl⁻···I angle approaches linearity there is an increase in the contribution from the sum of the chloride lone pair orbitals to V_{33}, since there is a greater degree of halogen bonding which further distorts this "p" orbital. Hence, we propose that the main contribution from the chloride lone pair orbital after 115°, which dictates the value of the chlorine quadrupolar coupling constant, may also be visualized as participating in electron donation to the σ-hole characteristic of the halogen bond. In the limit of an idealized model system, this interpretation of the value of C_Q can thus be taken as a measure of the halogen bonding interaction.

To validate the above hypothesis, the same NLMO analysis of V_{33} was conducted for each of the halogen-bonded complexes we studied experimentally (**1C**,**D** and **2C** for bromide and **1A**,**B** and **2B**,**E** for chloride; see Table 6). When the halogen-bonded environment is composed of two XB donors (iodine) interacting with a halide (I···X⁻···I motif), the same contributions are observed from the core and lone pair orbitals for the halide as were observed for the model system discussed above. Examination of the results plotted in Figure 6b shows that the calculated contributions for the halogen-bonded compounds follow the same trend for chloride (red) and bromide (black outline; the values are larger for this nuclide) and also follow the general trend established for the iodotrifluoromethane model. A change in sign is observed around 110−115° from the contributing lone pair orbitals (squares) to V_{33}, and a linear trend is observed for the contribution of the core orbital (diamonds) to V_{33}. The two dianionic species **1G** and **3G** have additional minor contributions from iodine lone pair orbitals to V_{33}. Compound **1E** has a different geometry. Its main contribution to V_{33} is from the chloride core and lone pair orbitals. The octahedral site in **1E** also has a very minor contribution from the iodine lone pair.

Finally, similar plots were prepared for the experimental values of V_{33} as a function of the I···X⁻···I angle determined from X-ray crystallography for the halogen-bonded complexes in this study (Figure 7b). Satisfyingly, when the I···X⁻···I angle increases, the largest principal component of the halide EFG tensor also increases. This is in agreement with the computa-

dx.doi.org/10.1021/ja5013239 | J. Am. Chem. Soc. 2014, 136, 6929−6942

Table 6. Analysis of Calculated Chlorine and Bromine EFG Tensor NLMO Contributions to the Largest Principal Component (V_{33}) in Halogen-Bonded Compounds

compd		core (X^-)	lone pair (X^-)	lone pair (I)[a]	sum[b]	V_{33}
1D		0.271	2.383		2.654	2.456
1C		0.277	2.381		2.658	2.452
2C		−0.165	−1.567		−1.732	−1.581
1G		0.247	2.127	−0.106	2.268	2.165
3G		0.116	0.876	−0.074	0.918	0.840
1A		−0.070	−0.809		−0.879	−0.831
1B		0.128	1.301		1.429	1.337
2E		0.067	0.757	−0.035	0.789	0.764
1E						
	site 1	0.029	0.262	−0.042	0.249	0.245
	site 2	−0.098	−0.999		−1.097	−0.968
2B						
	site 1	−0.068	−0.832		−0.900	−0.848
	site 2	0.108	1.215		1.323	1.246
	site 3	0.079	0.882		0.961	0.898

[a]Blank lines indicate that contributions are less than 5% of the sum. [b]Sum of "core" and "sum(LP)". Values obtained in this way differ from the total calculated V_{33} (final column) because not all of the contributions are printed.

tional study discussed above. The calculated asymmetry parameters are plotted as a function of the I···X^-···I angle extracted from the NLMO EFG tensor study in Figure 7a. The plot forms a bell shape over the range 80−180°. Overlaid on the same plot are the experimental values of the asymmetry parameters of the halogen-bonded complexes as a function of their experimentally determined I···X^-···I angles. Data for the chloride and bromide compounds both follow the predicted trend. From this we conclude that the experimentally observed asymmetry parameters are largely determined by the I···X^-···I angles, as suggested by ZORA DFT. A simple picture explaining the reasons behind this may be gleaned from a reinspection of the data in Figure 6 and Figure S20 (Supporting Information). When the I···X^-···I angle is 0°, the asymmetry parameter is 0 due to the cylindrical I···X^-···I symmetry, with the largest, unique EFG tensor component (V_{33}) oriented along the symmetry axis of the two halogen bonds. The chloride p orbital is oriented along this same axis and contributes to the electric field gradient in that direction. Similarly, when the I···X^-···I angle is 90° (the other limiting case), the V_{33} component lies perpendicular to the plane containing those three atoms, and the remaining components lying in the plane (V_{11} and V_{22}) are equal due to symmetry, resulting again in an asymmetry parameter of 0. For all intermediate angles, the values of V_{11} and V_{22} will not be equal due to the lower symmetry of the molecule, and the resulting asymmetry parameter will be nonzero. The asymmetry parameter reaches a maximum value of unity when the I···X^-···I angle is near the tetrahedral angle and the EFG tensor component V_{22} lies close to one of the iodine−chloride internuclear vectors (Figure S20).

Once this dependence on the local structure surrounding the halide was understood, it was possible to successfully simulate the ^{35}Cl NMR spectrum for [(*n*-Bu_4PCl)(*o*-DITFB)] (**2B**), where three distinct chloride ion sites are present. The I···Cl^-···I angles allowed for a good prediction of the asymmetry parameters for the three sites. For chloride site 1 $\theta_{I\cdots Cl^-\cdots I}$ = 112.0° and η_Q = 0.94(0.02), whereas the second chloride site has a much larger angle ($\theta_{I\cdots Cl^-\cdots I}$ = 144.5°) and the value of η_Q is 0.14(0.04). The third chloride site has an I···Cl^-···I angle between those for the two other sites (123.4°,) and η_Q = 0.72(0.10). This is a satisfying example of how the halogen-bonding environment surrounding the halide is manifested in the NMR parameters and highlights the advantages of a combined experimental−theoretical approach to evaluate the NMR parameters when there are multiple nonequivalent sites in the sample of interest, where site assignment may be ambiguous. In addition to the fundamental insights provided by this analysis, value also lies in the extension of the spectroscopic and computational methods employed herein to characterize halogen-bonded complexes where diffraction methods may not be amenable.

Given the clear-cut dependence of the halide quadrupolar asymmetry parameter on the I···Cl^-···I angle in halogen-bonded systems, it is of interest to compare this result to similar findings available for hydrogen bonds. The ^{2}H asymmetry parameters for deuterons in hydrogen bonds are known to deviate somewhat from 0 for nonlinear geometries,[86] but the dependence on structure can be complicated.[87] However, deuterons are electron acceptors in hydrogen bonds, whereas halide ions in halogen bonds are electron donors. A more apposite discussion is then of ^{17}O quadrupolar asymmetry parameters in hydrogen bonds of the form −N−H···O=C, where the oxygen acts as the electron donor. Wu and co-workers have demonstrated that $\eta_Q(^{17}O)$ decreases as $r_{N\cdots O}$ increases in hydrogen-bonded amides.[88] They have also shown that $\eta_Q(^{17}O)$ correlates with the hydrogen bond strength in a series of nucleic acid bases.[89] The full bell-shaped dependence noted presently for the halide quadrupolar asymmetry parameter is not seen for typical hydrogen bonds, likely simply

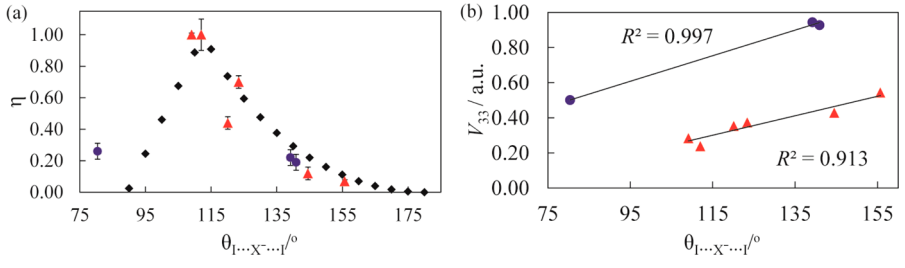

Figure 7. (a) Plot of quadrupolar asymmetry parameter versus I···Cl^-···I angle. The black diamonds represent the calculated values for ^{35}Cl in a F_3C−I···Cl^-···I−CF_3 model system. The red triangles and blue circles represent the experimental values for ^{35}Cl and ^{81}Br, respectively. (b) Plot of experimentally determined values of the largest component of the EFG tensor for ^{35}Cl (red triangles) and ^{81}Br (blue circles) versus the value of the I···X^-···I angle for compounds where two iodines interact with one halide anion. Solid lines show the best linear fit; $V_{33}(^{81}Br) = 0.0073(\theta_{I\cdots Br^-\cdots I}) - 0.0084$ and $V_{33}(^{35}Cl) = 0.0056(\theta_{I\cdots Cl^-\cdots I}) - 0.3383$.

dx.doi.org/10.1021/ja5013239 | J. Am. Chem. Soc. 2014, 136, 6929−6942

due to constraints on possible hydrogen bond geometries relative to what is seen for halogen bonds. Interestingly, however, Smith and co-workers reported[90] that computed ^{17}O EFG tensor orientations change with the strength of the hydrogen bond, analogously to what we have noted for halogen bonds (Figure S20, Supporting Information).

Additional computations resulted in the NMR parameters for ^{13}C, $^{35/37}$Cl, and $^{79/81}$Br for the compounds studied experimentally (see the Supporting Information for values). The models used consist of the simple halogen-bonding environment surrounding the halide (see Figure 1). The ^{13}C chemical shifts are overestimated by the calculations, consistent with our previous report on *p*-diiodotetrafluorobenzene complexes.[39] Nevertheless, in cases where distinct carbon resonances were observed experimentally, assignments to particular crystallographic sites were possible on the basis of differences in the carbon−iodine bond lengths. The calculations similarly overestimate the halide quadrupolar coupling parameters and show correlations of varying quality (Figure 8). Multiple reasons may explain this inability to reproduce the

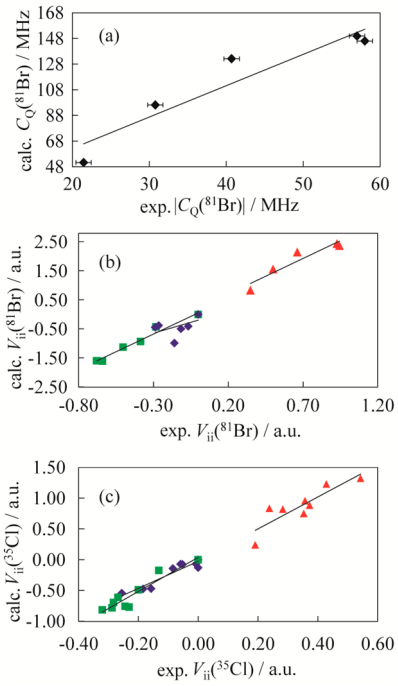

Figure 8. Plots of calculated versus experimental EFG tensors for bromine (a, b) and chlorine (c). The principal components V_{33}, V_{22}, and V_{11} are represented by the red triangles, green squares, and blue diamonds, respectively. Solid lines represent the best linear fit: (a) C_Q(calcd) = 2.4446[C_Q(exptl)] + 13.423, R^2 = 0.8933; (b) V_{11}(calcd) = 1.4926[V_{11}(exptl)] − 0.1952, R^2 = 2.2722, V_{22}(calcd) = 2.413-[V_{22}(exptl)] − 0.0548, R^2 = 0.9765, V_{33}(calcd) = 2.4446[V_{33}(exptl)] − 0.2185, R^2 = 0.8933; (c) V_{11}(calcd) = 2.1957[V_{11}(exptl)] − 0.0235, R^2 = 0.8826, V_{22}(calcd) = 2.7712[V_{22}(exptl)]− 0.041, R^2 = 0.8826, V_{33}(calcd) = 2.5907[V_{33}(exptl)] − 0.0148, R^2 = 0.7080.

experimental values precisely. For one, DFT calculations are performed in the gas phase and use a simple cluster model, whereas the compounds of interest crystallize in the solid state. A full treatment of the effect of the ions in the crystal lattice on the computed NMR parameters is possible with the gauge-including projector-augmented wave (GIPAW) DFT method[91] for calculations using periodic boundary conditions; however, for the present work many of the unit cells are too large for us to carry out such computations. Furthermore, we were interested in the NLMO analysis offered with the ZORA DFT method. The inclusion of relativistic effects via ZORA is important for computing the ^{13}C magnetic shielding tensors for carbon atoms bonded to iodine. Our calculations are carried out at 0 K, while the X-ray and NMR data are acquired at higher temperatures. This may also contribute to the discrepancies between the experimental and calculated values shown in Figure 8.

Since there is no single generally available computational approach at present which will simultaneously properly account for all of the aforementioned issues, compromises were made in choosing the best approach to address the problem at hand. The priorities for this study ((i) the ability to carry out an NLMO analysis to gain insight into the relationship between the halogen bond and the NMR observables and (ii) a proper consideration of relativistic effects on the NMR parameters) meant that the ZORA DFT method offered the best compromise.

CONCLUSIONS

A multifaceted study of halogen bonds has been presented. New halogen-bonded compounds without competing hydrogen bonds were prepared and characterized with X-ray crystallography and multinuclear magnetic resonance spectroscopy (^{13}C, $^{35/37}$Cl, $^{79/81}$Br). These iodobenzene-onium halide cocrystals exhibit C−I···X$^-$ distances and angles which allow them to be classified as moderately strongly halogen bonded compounds, as quantified by their reduced distance parameters, R_{XB}, of 0.79−0.91. The main conclusions of this study are as follows.

(1) From ^{13}C CP/MAS SSNMR, we observe an increase in the chemical shift of the *ipso* C−I carbon for the halogen *o*-diiodotetrafluorobenzene-bonded complexes in comparison to the starting materials; ^{13}C chemical shifts are therefore diagnostic of the strength of the halogen bond.

(2) From halogen SSNMR studies of a larger series of cocrystals, the NMR parameters of chloride and bromide anions were correlated to the local halogen-bonding environment. For example, octahedral and square-planar chloride ion coordination environments are clearly differentiated on the basis of their ^{35}Cl nuclear quadrupolar coupling constants. For C−I···X$^-$···I−C systems, the value of the halogen quadrupolar coupling constant correlates with the strength of the halogen bond.

(3) A natural localized molecular orbital DFT study afforded further chemical insight into the relationship among the quadrupolar NMR parameters of the halide ions, their local halogen bond environment, and an intuitive molecular orbital picture. The value of the quadrupolar coupling constant and the quadrupolar asymmetry parameter were found to be well-correlated with the I···X$^-$···I angle. Furthermore, this dependence could be explained, via both an NLMO analysis and a simpler MO picture, as arising largely from the contribution of a lone pair type orbital centered on the halide ion. The experimental asymmetry parameters follow the DFT trend and are highly correlated to the I···X$^-$···I angle.

(4) The correlations noted between the halide quadrupolar coupling parameters and the local halogen bond geometry are in qualitative agreement with the limited corresponding data available for the comparable electron donors in hydrogen bonds (i.e., ^{17}O quadrupolar parameters for oxygen); however, the data for halogen bonds cover a broader range of geometries.

dx.doi.org/10.1021/ja5013239 | J. Am. Chem. Soc. 2014, 136, 6929−6942

Overall, this work contributes to a chemically intuitive understanding of the connection between the geometry and electronic structure of halogen bonds and various NMR parameters with the aid of NLMO analysis. The experimental and computational methods employed here, as well as the insights gained, set the stage and hold promise for studying more complex halogen bond environments, such as those found in biomolecules,[92] gels,[9] receptors,[21] MOF-like framework materials,[11] and other systems where diffraction methods may provide an incomplete picture.

■ ASSOCIATED CONTENT

Supporting Information

Text, figures, tables, and CIF files giving additional experimental details, crystallographic data for **1E**, **2B**,**C**,**E**, **3G**, and *o*-DITFB, powder X-ray diffractograms, elemental analyses, images of the packing diagrams for the halogen-bonded compounds, full ^{13}C SSNMR spectra and assignments, NLMO analysis of XB compounds and ^{35}Cl EFG tensor orientations, additional halogen NMR spectra, and calculated NMR tensors. This material is available free of charge via the Internet at http://pubs.acs.org.

■ AUTHOR INFORMATION

Corresponding Author

*D.L.B.: tel, +1 613 562 5800 ext. 2018; fax, +1 613 562 5170; e-mail, dbryce@uottawa.ca.

Notes

The authors declare no competing financial interest.

■ ACKNOWLEDGMENTS

D.L.B. thanks the Natural Sciences and Engineering Research Council (NSERC) of Canada for funding and J.V.-G. thanks the Fonds de Recherche du Québec-Nature et Technologies (FRQNT) for a scholarship. Dr. Victor Terskikh, Dr. Eric Ye, and Dr. Glenn Facey are thanked for technical support. Access to the 900 MHz NMR spectrometer was provided by the National Ultrahigh-Field NMR Facility for Solids (Ottawa, Canada), a national research facility funded by the Canada Foundation for Innovation, the Ontario Innovation Trust, Recherche Québec, the National Research Council Canada, and Bruker BioSpin and is managed by the University of Ottawa (www.nmr900.ca). NSERC is acknowledged for a Major Resources Support grant.

■ REFERENCES

(1) Aakeröy, C. B. *Acta Crystallogr., Sect. B* **1997**, *B53*, 569−586.
(2) Metrangolo, P.; Meyer, F.; Pilati, T.; Resnati, G.; Terraneo, G. *Angew. Chem., Int. Ed.* **2008**, *47*, 6114−6127.
(3) Parisini, E.; Metrangolo, P.; Pilati, T.; Resnati, G.; Terraneo, G. *Chem. Soc. Rev.* **2011**, *40*, 2267−2278.
(4) Scholfield, M. R.; Vander Zanden, C. M.; Carter, M.; Ho, P. S. *Protein Sci.* **2013**, *22*, 139−152.
(5) Metrangolo, P.; Neukirch, H.; Pilati, T.; Resnati, G. *Acc. Chem. Res.* **2005**, *38*, 386−395.
(6) Gamez, P.; Mooibroek, T. J.; Teat, S. J.; Reedijk, J. *Acc. Chem. Res.* **2007**, *40*, 435−444.
(7) Gorteau, V.; Bollot, G.; Mareda, J.; Perez-Velasco, A.; Matile, S. *J. Am. Chem. Soc.* **2006**, *128*, 14788−14789.
(8) Takeuchi, T.; Matile, S. *J. Am. Chem. Soc.* **2009**, *131*, 18048−18049.
(9) Meazza, L.; Foster, J. A.; Fucke, K.; Metrangolo, P.; Resnati, G.; Steed, J. W. *Nat. Chem.* **2013**, *5*, 42−47.
(10) Yamamoto, H. M.; Yamaura, J.-I.; Kato, R. *J. Am. Chem. Soc.* **1998**, *120*, 5905−5913.
(11) Lieffrig, J.; Jeannin, O.; Fourmigué, M. *J. Am. Chem. Soc.* **2013**, *135*, 6200−6210.
(12) Metrangolo, P.; Carcenac, Y.; Lahtinen, M.; Pilati, T.; Rissanen, K.; Vij, A.; Resnati, G. *Science* **2009**, *323*, 1461−1464.
(13) El-Sheshtawy, H. S.; Bassil, B. S.; Assaf, K. I.; Kortz, U.; Nau, W. M. *J. Am. Chem. Soc.* **2012**, *134*, 19935−19941.
(14) Auffinger, P.; Hays, F. A.; Westhof, E.; Ho, P. S. *Proc. Natl. Acad. Sci. U.S.A.* **2004**, *101*, 16789−16794.
(15) Manna, D.; Mugesh, G. *J. Am. Chem. Soc.* **2012**, *134*, 4269−4279.
(16) Sarwar, M. G.; Ajami, D.; Theodorakopoulos, G.; Petsalakis, I. D.; Rebek, J., Jr. *J. Am. Chem. Soc.* **2013**, *135*, 13672−13675.
(17) Hardegger, L. A.; Kuhn, B.; Spinnler, B.; Anselm, L.; Ecabert, R.; Stihle, M.; Gsell, B.; Thoma, R.; Diez, J.; Benz, J.; Plancher, J.−M.; Hartmann, G.; Banner, D. W.; Haap, W.; Diederich, F. *Angew. Chem., Int. Ed.* **2011**, *50*, 314−318.
(18) Lu, Y.; Shi, T.; Wang, Y.; Yang, H.; Yan, X.; Luo, X.; Jiang, H.; Zhu, W. *J. Med. Chem.* **2009**, *52*, 2854−2862.
(19) (a) Wilcken, R.; Zimmermann, M. O.; Lange, A.; Joerger, A. C.; Boeckler, F. M. *J. Med. Chem.* **2013**, *56*, 1363−1398. (b) Wilcken, R.; Liu, X.; Zimmermann, M. O.; Rutherford, T. J.; Fersht, A. R.; Joerger, A. C.; Boeckler, F. M. *J. Am. Chem. Soc.* **2012**, *134*, 6810−6818. (c) Lemke, C. T.; Goudreau, N.; Zhao, S.; Hucke, O.; Thibeault, D.; Llinàs-Brunet, M.; White, P. W. *J. Biol. Chem.* **2011**, *286*, 11434−11443.
(20) Kilah, N. L.; Wise, M. D.; Serpell, C. J.; Thompson, A. L.; White, N. G.; Christensen, K. E.; Beer, P. D. *J. Am. Chem. Soc.* **2010**, *132*, 11893−11895.
(21) Chudzinski, M. G.; McClary, C. A.; Taylor, M. S. *J. Am. Chem. Soc.* **2011**, *133*, 10559−10567.
(22) Zapata, F.; Caballero, A.; White, N. G.; Claridge, T. D. W.; Costa, P. J.; Félix, V.; Beer, P. D. *J. Am. Chem. Soc.* **2012**, *134*, 11533−11541.
(23) Gilday, L. C.; Lang, T.; Caballero, A.; Costa, P. J.; Félix, V.; Beer, P. D. *Angew. Chem., Int. Ed.* **2013**, *52*, 4356−4360.
(24) Jentzsch, A. V.; Emery, D.; Mareda, J.; Nayak, S. K.; Metrangolo, P.; Resnati, G.; Sakai, N.; Matile, S. *Nat. Commun.* **2012**, *3:905*, 1−8.
(25) Walter, S. M.; Kniep, F.; Herdtweck, E.; Huber, S. M. *Angew. Chem., Int. Ed.* **2011**, *50*, 7187−7191.
(26) Desiraju, G. R.; Ho, P. S.; Kloo, L.; Legon, A. C.; Marquardt, R.; Metrangolo, P.; Politzer, P. A.; Resnati, G.; Rissanen, K. *Pure Appl. Chem.* **2013**, *85*, 1711−1713.
(27) Politzer, P.; Murray, J. S. *ChemPhysChem.* **2013**, *14*, 278−294.
(28) Clark, T.; Hennemann, M.; Murray, J. S.; Politzer, P. *J. Mol. Model.* **2007**, *13*, 291−296.
(29) Fourmigué, M. *Curr. Opin. Solid State Mater. Sci.* **2009**, *13*, 36−45.
(30) Mooibroek, T. J.; Gamez, P. *CrystEngComm* **2013**, *15*, 4565−4570.
(31) Legon, A. C. *Phys. Chem. Chem. Phys.* **2010**, *12*, 7736−7747.
(32) Legon, A. C. *Halogen Bonding: Fundamentals and Applications*; Springer: Berlin, 2008; Structure and Bonding Vol. *126*, pp 17−64.
(33) Legon, A. C. *Angew. Chem., Int. Ed.* **1999**, *38*, 2686−2714.
(34) Bertrán, J. F.; Rodríguez, M. *Org. Magn. Reson.* **1979**, *12*, 92−94.
(35) (a) Rege, P. D.; Malkina, O. L.; Goroff, N. S. *J. Am. Chem. Soc.* **2002**, *124*, 370−371. (b) Webb, J. A.; Klijn, J. E.; Hill, P. A.; Bennett, J. L.; Goroff, N. S. *J. Org. Chem.* **2004**, *69*, 660−664.
(36) (a) Carlsson, A.-C. C.; Gräfenstein, J.; Budnjo, A.; Laurila, J. L.; Bergquist, J.; Karim, A.; Kleinmaier, R.; Brath, U.; Erdélyi, M. *J. Am. Chem. Soc.* **2012**, *134*, 5706−5715. (b) Carlsson, A.-C. C.; Uhrbom, M.; Karim, A.; Brath, U.; Gräfenstein, J.; Erdélyi, M. *CrystEngComm* **2013**, *15*, 3087−3092.
(37) Weingarth, M.; Raouafi, N.; Jouvelet, B.; Duma, L.; Bodenhausen, G.; Boujlel, K.; Schöllhorn, B.; Tekely, P. *Chem. Commun.* **2008**, 5981−5983.
(38) Bouchmella, K.; Dutremez, S. G.; Alonso, B.; Mauri, F.; Gervais, C. *Cryst. Growth. Des.* **2008**, *8*, 3941−3950.

(39) Viger-Gravel, J.; Leclerc, S.; Korobkov, I.; Bryce, D. L. *CrystEngComm* **2013**, *15*, 3168−3177.
(40) Viger-Gravel, J.; Korobkov, I.; Bryce, D. L. *Cryst. Growth Des.* **2011**, *11*, 4984−4995.
(41) Widdifield, C. M.; Cavallo, G.; Facey, G. A.; Pilati, T.; Lin, J.; Metrangolo, P.; Resnati, G.; Bryce, D. L. *Chem. Eur. J.* **2013**, *19*, 11949−11962.
(42) Attrell, R. J.; Widdifield, C. M.; Korobkov, I.; Bryce, D. L. *Cryst. Growth Des.* **2012**, *12*, 1641−1653.
(43) Chapman, R. P.; Widdifield, C. M.; Bryce, D. L. *Prog. Nucl. Magn. Reson. Spectrosc.* **2009**, *55*, 215−237.
(44) Bryce, D. L.; Widdifield, C. M.; Chapman, R. P.; Attrell, R. J. Chlorine, Bromine, and Iodine Solid-State NMR. In *Encyclopedia of Magnetic Resonance*; Wiley: Chichester, U.K., 2007−2011.
(45) Burgess, K. M. N.; Korobkov, I.; Bryce, D. L. *Chem. Eur. J.* **2012**, *18*, 5748−5758.
(46) Chapman, R. P.; Bryce, D. L. *Phys. Chem. Chem. Phys.* **2009**, *11*, 6987−6998.
(47) Widdifield, C. M.; Bryce, D. L. *J. Phys. Chem. A* **2010**, *114*, 2102−2116.
(48) Perras, F. A.; Bryce, D. L. *Angew. Chem., Int. Ed.* **2012**, *51*, 4227−4230.
(49) Hamaed, H.; Pawlowski, J. M.; Cooper, B. F. T.; Fu, R.; Eichhorn, S. H.; Schurko, R. W. *J. Am. Chem. Soc.* **2008**, *130*, 11056−11065.
(50) Alonso, B.; Mineva, T.; Innocenzi, P.; Trimmel, G.; Stubenrauch, K.; Melnyk, I.; Zub, Y.; Fayon, F.; Florian, P.; Massiot, D. *C. R. Chim.* **2010**, *13*, 431−442.
(51) (a) Bondi, A. *J. Phys. Chem.* **1964**, *68*, 441−451. (b) Shannon, R. D. *Acta Crystallogr., Sect. A* **1976**, *A32*, 751−767.
(52) Troff, R. W.; Mäkelä, T.; Topić, F.; Valkonen, A.; Raatikainen, K.; Rissanen, K. *Eur. J. Org. Chem.* **2013**, 1617−1637.
(53) Autschbach, J.; Zheng, S.; Schurko, R. W. *Concepts Magn. Reson., Part A* **2010**, *36*, 84−126.
(54) O'Dell, L. A.; Schurko, R. W.; Harris, K. J.; Autschbach, J.; Ratcliffe, C. I. *J. Am. Chem. Soc.* **2011**, *133*, 527−546.
(55) Rossini, A. J.; Mills, R. W.; Briscoe, G. A.; Norton, E. L.; Geier, S. J.; Hung, I.; Zheng, S.; Autschbach, J.; Schurko, R. W. *J. Am. Chem. Soc.* **2009**, *131*, 3317−3330.
(56) *APEX Software Suite v.2010*; Bruker AXS: Madison, WI, 2005.
(57) Blessing, R. H. *Acta Crystallogr., Sect. A* **1995**, *A51*, 33−38.
(58) Sheldrick, G. M. *Acta Crystallogr., Sect. A* **2008**, *A64*, 112−122.
(59) (a) Metz, G.; Wu, X.; Smith, S. O. *J. Magn. Reson., Ser. A* **1994**, *110*, 219−227. (b) Schaefer, J.; Stejskal, E. O. *J. Am. Chem. Soc.* **1976**, *98*, 1031−1032.
(60) Fung, B. M.; Khitrin, A. K.; Ermolaev, K. *J. Magn. Reson.* **2000**, *142*, 97−101.
(61) O'Dell, L. A.; Schurko, R. W. *Chem. Phys. Lett.* **2008**, *464*, 97−102.
(62) Massiot, D.; Farnan, I.; Gautier, N.; Trumeau, D.; Trokiner, A.; Coutures, J. P. *Solid State Nucl. Magn. Reson.* **1995**, *4*, 241−248.
(63) (a) Solomon, I. *Phys. Rev.* **1958**, *110*, 61−65. (b) Weisman, I. D.; Bennett, L. H. *Phys. Rev.* **1969**, *181*, 1341−1352. (c) Bodart, P. R.; Amoureux, J.-P.; Dumazy, Y.; Lefort, R. *Mol. Phys.* **2000**, *98*, 1545−1551.
(64) Eichele, K.; Wasylishen, R. E. *WSOLIDS1 NMR Simulation Package, version 1.20.15*; Universitat Tübingen, Tübingen, Germany, 2001.
(65) Massiot, D.; Fayon, F.; Capron, M.; King, I.; Le Calvé, S.; Alonso, B.; Durand, J.-O.; Bujoli, B.; Gan, Z.; Hoatson, G. *Magn. Reson. Chem.* **2002**, *40*, 70−76.
(66) Frisch, M. J.; Trucks, G. W.; Schlegel, H. B.; Scuseria, G. E.; Robb, M. A.; Cheeseman, J. R.; Montgomery, J. A., Jr.; Vreven, T.; Kudin, K. N.; Burant, J. C.; Millam, J. M.; Iyengar, S. S.; Tomasi, J.; Barone, V.; Mennucci, B.; Cossi, M.; Scalmani, G.; Rega, N.; Petersson, G. A.; Nakatsuji, H.; Hada, M.; Ehara, M.; Toyota, K.; Fukuda, R.; Hasegawa, J.; Ishida, M.; Nakajima, T.; Honda, Y.; Kitao, O.; Nakai, H.; Klene, M.; Li, X.; Knox, J. E.; Hratchian, H. P.; Cross, J. B.; Bakken, V.; Adamo, C.; Jaramillo, J.; Gomperts, R.; Stratmann, R. E.; Yazyev, O.; Austin, A. J.; Cammi, R.; Pomelli, C.; Ochterski, J. W.; Ayala, P. Y.; Morokuma, K.; Voth, G. A.; Salvador, P.; Dannenberg, J. J.; Zakrzewski, V. G.; Dapprich, S.; Daniels, A. D.; Strain, M. C.; Farkas, O.; Malick, D. K.; Rabuck, A. D.; Raghavachari, K.; Foresman, J. B.; Ortiz, J. V.; Cui, Q.; Baboul, A. G.; Clifford, S.; Cioslowski, J.; Stefanov, B. B.; Liu, G.; Liashenko, A.; Piskorz, P.; Komaromi, I.; Martin, R. L.; Fox, D. J.; Keith, T.; Al-Laham, M. A.; Peng, C. Y.; Nanayakkara, A.; Challacombe, M.; Gill, P. M. W.; Johnson, B.; Chen, W.; Wong, M. W.; Gonzalez, C.; Pople, J. A. *Gaussian 09, rev. A.02*; Gaussian, Inc., Wallingford, CT, 2009.
(67) Zhang, Y.; Yang, W. *Phys. Rev. Lett.* **1998**, *80*, 890.
(68) Chong, D. P. *Mol. Phys.* **2005**, *103*, 749−761.
(69) van Lenthe, E.; Baerends, E. J. *J. Comput. Chem.* **2003**, *24*, 1142−1156.
(70) Adiga, S.; Aebi, D.; Bryce, D. L. *Can. J. Chem.* **2007**, *85*, 496−505.
(71) Jameson, A. K.; Jameson, C. J. *Chem. Phys. Lett.* **1987**, *134*, 461−466.
(72) Gee, M.; Wasylishen, R. E.; Laaksonen, A. *J. Phys. Chem. A* **1999**, *103*, 10805−10812.
(73) Deverell, C.; Richards, R. E. *Mol. Phys.* **1969**, *16*, 421−439.
(74) Loewenstein, A.; Shporer, M. *J. Chem. Soc., Chem. Commun.* **1968**, 214−215.
(75) (a) Raatikainen, K.; Rissanen, K. *CrystEngComm* **2011**, *13*, 6972−6977. (b) Johnson, M. T.; Džolić, Z.; Cetina, M.; Wendt, O. F.; Öhrström, L.; Rissanen, K. *Cryst. Growth Des.* **2012**, *12*, 362−368.
(76) (a) Dance, I.; Scudder, M. *Chem. Eur. J.* **1996**, *2*, 481−486. (b) Dance, I.; Scudder, M. *J. Chem. Soc., Chem. Commun.* **1995**, 1039−1040.
(77) Abate, A.; Biella, S.; Cavallo, G.; Meyer, F.; Neukirch, H.; Metrangolo, P.; Pilati, T.; Resnati, G.; Terraneo, G. *J. Fluorine Chem.* **2009**, *130*, 1171−1177.
(78) Grebe, J.; Geiseler, G.; Harms, K.; Dehnicke, K. *Z. Naturforsch., B* **1999**, *54b*, 77−86.
(79) Desiraju, G. R.; Steiner, T. *The Weak Hydrogen Bond*; Oxford University Press: Oxford, U.K., 1999; IUCr Monographs on Crystallography *9*.
(80) Kaupp, M.; Malkina, O. L.; Malkin, V. G.; Pyykkö, P. *Chem. Eur. J.* **1998**, *4*, 118−126.
(81) Gordon, P. G.; Brouwer, D. H.; Ripmeester, J. A. *ChemPhysChem* **2010**, *11*, 260−268.
(82) Widdifield, C. M.; Chapman, R. P.; Bryce, D. L. *Ann. Rep. Nucl. Magn. Reson. Spectrosc.* **2009**, *66*, 195−326.
(83) Chapman, R. P.; Hiscock, J. R.; Gale, P. A.; Bryce, D. L. *Can. J. Chem.* **2011**, *89*, 822−834.
(84) Kentgens, A. P. M. *Geoderma* **1997**, *80*, 271−306.
(85) Pinter, B.; Nagels, N.; Herrebout, W. A.; De Proft, F. *Chem. Eur. J.* **2013**, *19*, 519−530.
(86) Brown, T. L.; Butler, L. G.; Curtin, D. Y.; Hiyama, Y.; Paul, I. C.; Wilson, R. B. *J. Am. Chem. Soc.* **1982**, *104*, 1172−1177.
(87) Michal, C. A.; Wehman, J. C.; Jelinski, L. W. *J. Magn. Reson., Ser. B* **1996**, *111*, 31−39.
(88) Yamada, K.; Dong, S.; Wu, G. *J. Am. Chem. Soc.* **2000**, *122*, 11602−11609.
(89) Wu, G.; Dong, S.; Ida, R.; Reen, N. *J. Am. Chem. Soc.* **2002**, *124*, 1768−1777.
(90) Wong, A.; Pike, K. J.; Jenkins, R.; Clarkson, G. J.; Anupõld, T.; Howes, A. P.; Crout, D. H. G.; Samoson, A.; Dupree, R.; Smith, M. E. *J. Phys. Chem. A* **2006**, *110*, 1824−1835.
(91) (a) Pickard, C. J.; Mauri, F. *Phys. Rev. B* **2001**, *63*, 245101−13. (b) Yates, J. R.; Pickard, C. J.; Mauri, F. *Phys. Rev. B* **2007**, *76*, 024401−11. (c) Profeta, M.; Mauri, F.; Pickard, C. J. *J. Am. Chem. Soc.* **2003**, *125*, 541−548. (d) Clark, S. J.; Segall, M. D.; Pickard, C. J.; Hasnip, P. J.; Probert, M. I. J.; Refson, K.; Payne, M. C. *Z. Kristallogr.* **2005**, *220*, 567−570.
(92) Carter, M.; Voth, A. R.; Scholfield, M. R.; Rummel, B.; Sowers, L. C.; Ho, P. S. *Biochemistry* **2013**, *52*, 4891−4903.